SANDIA REPORT
SAND2006-7937
Unlimited Release
Printed January 2007

Defect-Related Internal Dissipation in Mechanical Resonators and the Study of Coupled Mechanical Systems

John P. Sullivan, Normand A. Modine, David A. Czaplewski, Thomas A. Friedmann, Joel R. Wendt, Nelson Sepulveda, and Dean M. Aslam

Prepared by
Sandia National Laboratories
Albuquerque, New Mexico 87185 and Livermore, California 94550

Sandia is a multiprogram laboratory operated by Sandia Corporation,
a Lockheed Martin Company, for the United States Department of Energy's
National Nuclear Security Administration under Contract DE-AC04-94AL85000.

Issued by Sandia National Laboratories, operated for the United States Department of Energy by Sandia Corporation.

Available to DOE and DOE contractors from
U.S. Department of Energy
Office of Scientific and Technical Information
P.O. Box 62
Oak Ridge, TN 37831

Telephone: (865) 576-8401
Facsimile: (865) 576-5728
E-Mail: reports@adonis.osti.gov
Online ordering: http://www.osti.gov/bridge

Available to the public from
U.S. Department of Commerce
National Technical Information Service
5285 Port Royal Rd.
Springfield, VA 22161

Telephone: (800) 553-6847
Facsimile: (703) 605-6900
E-Mail: orders@ntis.fedworld.gov
Online order: http://www.ntis.gov/help/ordermethods.asp?loc=7-4-0#online

SAND2006-7937
Unlimited Release
Printed January 2007

Defect-Related Internal Dissipation in Mechanical Resonators and the Study of Coupled Mechanical Systems

J. P. Sullivan and N. A. Modine
CINT Science Department

D. A. Czaplewski
Advanced MEMS Department

T. A. Friedmann
Nanostructure and Semiconductor Physics Department

J. R. Wendt
Photonic Microsystems Technology Department

Sandia National Laboratories
P.O. Box 5800
Albuquerque, NM 87185

and

N. Sepulveda[1] and D. M. Aslam[2]
[1]University of Puerto Rico, Mayaguez, PR
[2]Michigan State University, Lansing, MI

Abstract

Understanding internal dissipation in resonant mechanical systems at the micro- and nanoscale is of great technological and fundamental interest. Resonant mechanical systems are central to many sensor technologies, and microscale resonators form the basis of a variety of scanning probe microscopies. Furthermore, coupled resonant mechanical systems are of great utility for the study of complex dynamics in systems ranging from biology to electronics to photonics. In this work, we report the detailed experimental study of internal dissipation in micro- and nanomechanical oscillators fabricated from amorphous and crystalline diamond materials, atomistic modeling of dissipation in amorphous, defect-free, and defect-containing crystalline silicon, and experimental work on the properties of one-dimensional and two-dimensional coupled mechanical oscillator arrays. We have identified that internal dissipation in most micro- and nanoscale oscillators is limited by defect relaxation processes, with large differences in the nature of the defects as the local order of the material ranges from amorphous to crystalline. Atomistic simulations also showed a dominant role of defect relaxation processes in controlling internal dissipation. Our studies of one-dimensional and two-dimensional coupled oscillator arrays revealed that it is possible to create mechanical systems that should be ideal for the study of non-linear dynamics and localization.

[Intentionally Left Blank]

CONTENTS

1.0 Executive Summary

The work in this report includes (1) a detailed experimental study of internal dissipation in micro- and nanomechanical oscillators fabricated in amorphous and crystalline diamond materials, (2) atomistic modeling of dissipation in amorphous, crystalline, and crystalline + defect silicon, and (3) experimental work on the properties of one-dimensional and two-dimensional coupled mechanical oscillator arrays.

Internal dissipation mechanisms were assessed in tetrahedral amorphous carbon (ta-C) films by measuring the quality factor (Q) of fixed-free beams and torsional oscillators with varying dimensions over a temperature range of 300 to 1023 K. Defect-controlled dissipation was observed with typical Qs of 4×10^3. Assuming these defects exhibit a Debye like relaxation and are thermally activated, we calculated the distribution of activation energies for defect relaxation in this system. The activation energies for defect relaxation were found to range from less than 0.5 eV to over 1.9 eV, and the defect relaxation was found to be only slightly sensitive to vibrational strain state (flexure vs. torsion). In addition to characterizing the internal dissipation in this system, we have performed the first measurements of the temperature-dependent mechanical properties of ta-C films. Flexural and torsional oscillators were fabricated out of ta-C, and the resonant frequencies were measured in the temperature range of 300 K to 873 K. At room temperature, the Young's modulus, shear modulus, and Poisson's ratio were found to be 662 ± 24 GPa, 275 ± 7 GPa and 0.202 ± 0.054, respectively. We also measured the temperature dependent behavior of the thermal expansion coefficient of ta-C, and a room temperature value of $1.47 \times 10^{-6} \pm 2.5 \times 10^{-7}$ was observed.

In contrast to amorphous carbon films, polycrystalline diamond (poly-C) resonators were found to exhibit much higher Qs. The highest Q values were observed for undoped poly-C films grown at 1053 K. For boron doped poly-C films or poly-C films grown at a growth temperature of 873 K, lower Qs were observed. The doped poly-C film exhibited a peak in dissipation at 673 K, suggesting the existence of a dominant defect in these films that may be related to boron doping. The high Qs in all of the poly-C films suggest lower defect densities than found in amorphous films, which may be expected on the basis of the much higher degree of order in crystalline materials. This suggests that the amorphous network of amorphous carbon is able to support a large number of defect relaxation processes that may involve individual or large collections of atoms. The temperature dependence of the poly-C resonators was also examined, and a temperature coefficient of resonance frequency in the range of -1.59×10^{-5} to -2.56×10^{-5} K^{-1} was observed. We also report the smallest patterned poly-C nanoresonator structure, a cantilever resonator that is 100 nm wide, 0.7 μm thick and 40 μm long.

Numerical simulation of internal dissipation in amorphous silicon, defect-free crystalline silicon, and defect-containing crystalline silicon nanoresonators revealed strong enhancement of dissipation in the presence of defects. Amorphous systems showed quality factors more than two orders of magnitude lower than the crystalline system at frequencies approaching 1 THz. A model study involving a single split interstitial defect in crystalline silicon revealed that there is a strong reduction in quality factor up to 60% with the existence of a single defect. A temperature-dependent study of internal dissipation in this system showed that the internal dissipation is higher over the entire temperature range that was studied (300 K to 700 K) for the system with defect, but no strong defect resonance was observed.

Coupled oscillator arrays, including 1D arrays of cantilever oscillators and 2D arrays of nodes and springs, were fabricated out of amorphous and polycrystalline diamond materials.

The 2D arrays were fabricated as square lattices of 10 × 10 and 100 × 100 elements having tungsten proof masses at each element. These arrays were fabricated to be ideal (free of defects), and experimental testing revealed a series of drumhead vibration modes. Simulations of arrays containing regions of disorder revealed that mode localization should be observable in defect-containing arrays. Studies to confirm localization in these mechanical systems have been undertaken.

2.0 Introduction

2.1 Background

Small resonant mechanical systems are attractive for applications in sensing, electrical signal processing, and basic research on the dynamics of coupled systems. One of the appeals of mechanical systems is the inherently high sensitivity of mechanical systems to small forces. For example, the force constant (amount of force required to produce a unit of displacement) of a cantilever resonator scales as the cube of the ratio of the cantilever thickness to cantilever length (t/L):

$$K = \frac{E_Y w}{4}\left(\frac{t}{L}\right)^3, \tag{2.1}$$

where K is the force constant, E_Y is the elastic modulus, and w is the cantilever width. For example, a concrete bridge span that is 1 m thick, 10 m wide, and cantilevered 100 m over a cliff would have a force constant of 75,000 N/m (one person standing at the edge of this span would produce a deflection of about 1 cm). In comparison, a. typical cantilever sensor used in atomic force microscopy has a force constant of 1 N/m. These cantilever sensors are able to detect single atom steps on surfaces (approaching piconewton force sensitivity). In this work, we have fabricated nanoscale cantilevers with dimensions as small as 100 nm thick, 40 μm long, and 0.7 μm wide. These particular cantilevers were fabricated using the stiffest material known (crystalline diamond, which has $E_Y \sim 1050$ GPa or more than 35 times higher than high strength concrete), but the force constants are as low as 0.003 N/m (see Fig. 2.1). Clearly, it is possible to achieve extremely high levels of force sensitivity using small mechanical systems.

There is a problem, however. Mechanical systems with low force constants are also susceptible to high thermal noise. The amplitude of vibration due to thermal noise is easily estimated:

$$\left\langle x^2 \right\rangle^{1/2} = \sqrt{\frac{k_B T}{K}}, \tag{2.2}$$

where $\langle x^2 \rangle^{1/2}$ is the mean displacement, and $k_B T$ is the thermal energy. At room temperature $\langle x^2 \rangle^{1/2}$ is about 1 nm in the polycrystalline diamond nanoresonator. To overcome this limitation, it is desirable to use resonant mechanical systems where the static displacement of the end of the cantilever is not the response of interest. In a resonant mechanical system, detection is achieved by measuring shifts in resonance frequency or changes in the phase angle of the oscillator when compared to a constant driving signal. The difficulty with this approach is that the resonator needs to be of low internal dissipation (low damping) – the quality factor, Q, of the resonator must be high. In fact, the minimum detectable force for a resonant mechanical system scales as $Q^{-1/2}$. Therefore, a critical aspect of designing high sensitivity mechanical systems is designing a system with high Q. Unfortunately, our understanding of what controls Q in micro- and nanomechanical systems is extremely limited.

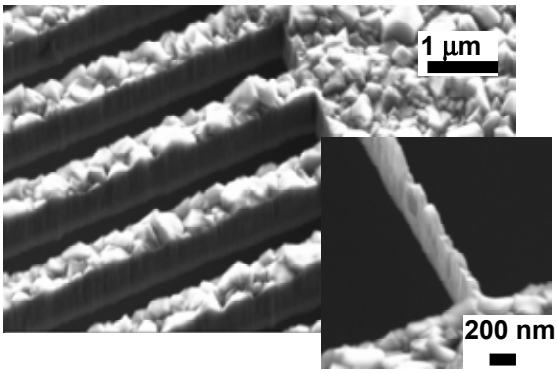

Fig. 2.1. Some examples of polycrystalline diamond nanomechanical resonator structures.

2.2 Project Structure

The work in this project is focused in two parts: (1) understanding fundamental mechanisms that control internal dissipation in resonant micro- and nanomechanical systems, and (2) exploring systems of coupled mechanical systems – which ultimately may lead to sensing solutions that are not dependent on the existence of high Q resonators [1-5]. This report is organized into several sections. In the following three sections, we describe the experimental measurement of internal dissipation mechanisms in amorphous and polycrystalline diamond materials. These material systems permit us to contrast the nature of the dissipation mechanism in a material lacking crystalline order and long range defects (dislocations, grain boundaries, etc.) with the same elemental material but one that has local crystalline order and long range defects, such as grain boundaries, see Fig. 2.2 for a contrast of the atomic structure of these materials. In both cases, we observe that internal dissipation is controlled by defects in the material and not by intrinsic dissipation mechanisms, such as thermoelastic dissipation. However, the distribution of defect relaxation energies and the total magnitude of the dissipation is very different between the two systems.

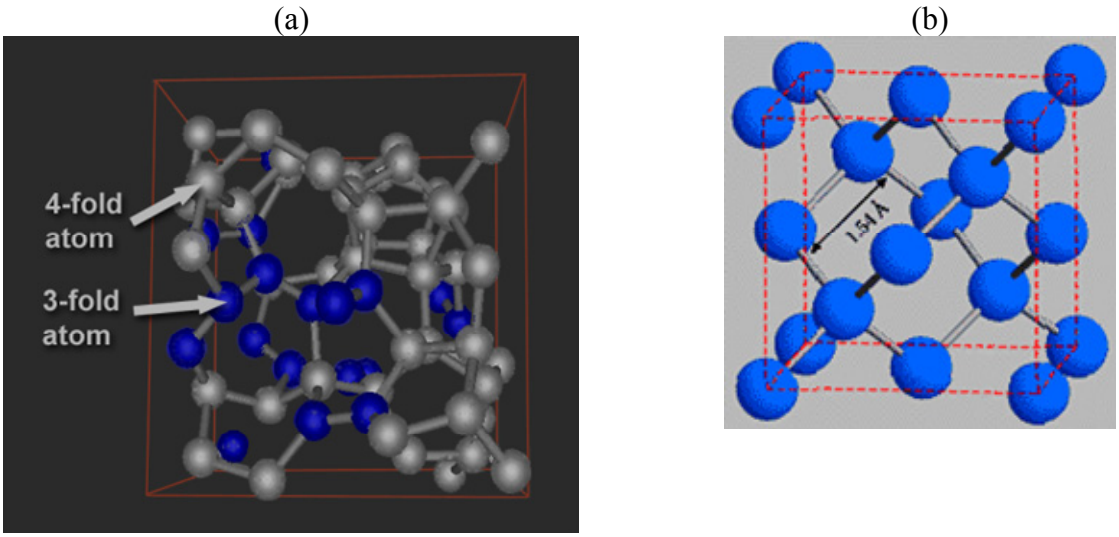

Fig. 2.2. (a) Amorphous tetrahedrally-coordinated carbon (ta-C), as determined from calculations [6], and (b) crystalline diamond [7]. In ta-C, the local bonding is similar to that of diamond (4-fold coordinated carbon atoms), but there is no long-range order.

Since the fabrication of these mechanical resonators is not discussed in detail elsewhere, it is briefly described here. The resonant mechanical systems were fabricated using surface micromachining processes that are summarized in Fig. 2.3. In brief, the material of interest, e.g. tetrahedral amorphous carbon (ta-C) or polycrystalline diamond, is deposited on to a sacrificial layer on silicon (typically, SiO_2). A thin film of Al is then patterned on the surface of the film using optical lithography or e-beam lithography followed by metal lift-off. The structure is then placed in an O_2/Ar plasma to etch through the carbon material in areas that are not covered by the Al film. The Al film and the underlying sacrificial layer of SiO_2 are then removed in a wet etch process using HF or NH_4OH/HF. The structures are then dried in N_2, and a rapid thermal anneal is briefly used to further dry the structures and enhance their release from the substrate. Due to the hydrophobic nature of carbon films, this process generally leads to fully-released structures without the need for any subsequent release steps, such as the use of self-assembled monolayer coatings (SAMS) or super-critical CO_2 drying.

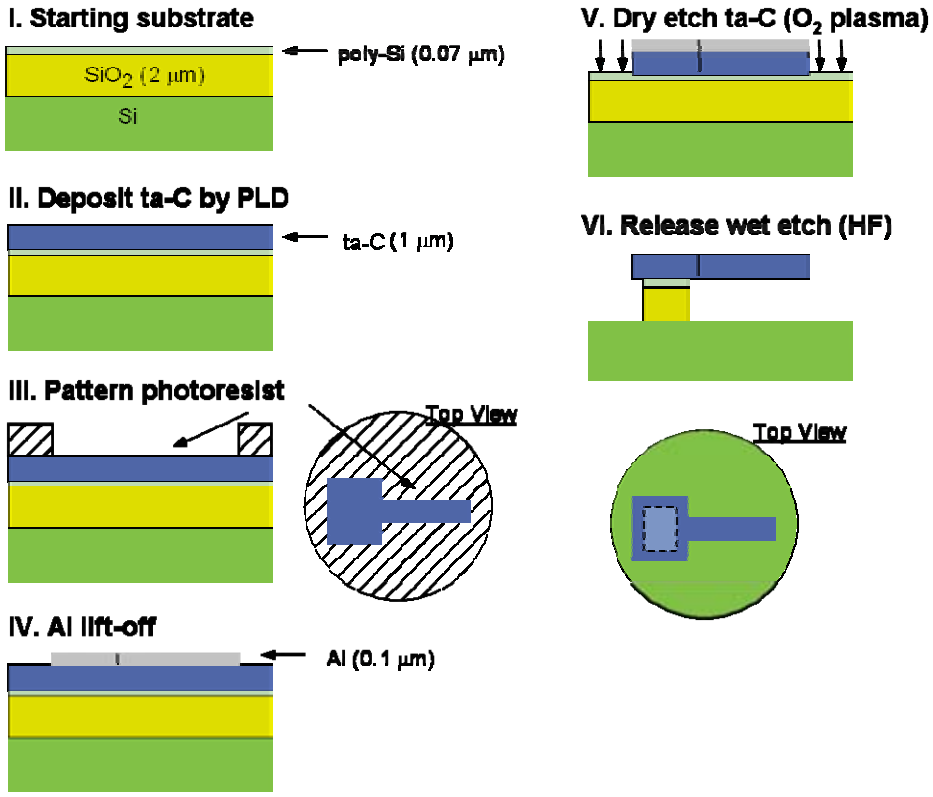

Fig. 2.3. Process flow for the creation of micro- and nanomechanical structures in carbon.

In the section following the experimental measurements of dissipation, we discuss a theoretical treatment of internal dissipation using silicon as an archetypal material. The simulations are atomistic, using a molecular dynamics approach to directly monitor the decay of vibrational states in the system. The simulations involved amorphous, crystalline, and crystalline + defect systems, wherein the nature of the dissipation process could be studied and compared.

In the last research section of this report, we discuss our experimental work on coupled mechanical systems. Our fabrication of coupled oscillator arrays culminated in the creation of 100 × 100 element oscillator arrays employing amorphous carbon and islands of tungsten (see

Fig. 2.4). Our initial work in this area has shown that the physics of coupled mechanical systems can be quite rich, suggesting the promise of this approach for the creation of unique types of sensing structures where the response of the array greatly exceeds the response of an individual element of the array. This is an exciting area of future work.

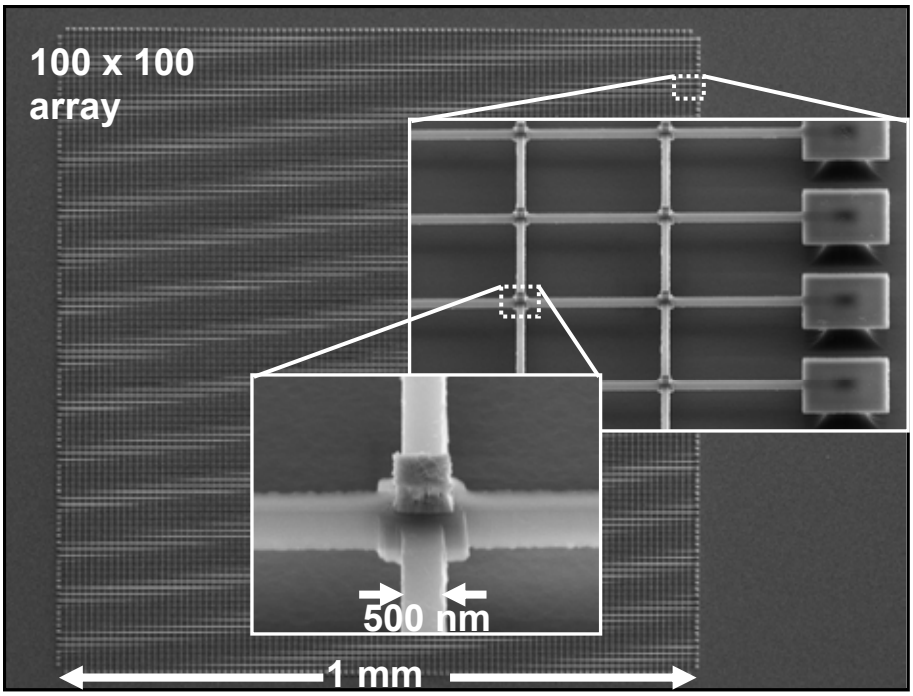

Fig. 2.4. A 100 × 100 coupled oscillator array consisting of a grid of amorphous carbon topped by islands of tungsten at the grid nodes.

2.3 References

[1] D. A. Czaplewski, J. P. Sullivan, T. A. Friedmann, and J. R. Wendt, Appl. Phys. Lett. **87**, 161915 (2005).

[2] N. Sepulveda, D. Aslam, and J. P. Sullivan, Diamond and Rel. Mater. **15**, 398 (2006).

[3] D. A. Czaplewski, J. P. Sullivan, T. A. Friedmann, J. R. Wendt, Diamond and Rel. Mater. **15**, 309 (2006).

[4] Nelson Sepulveda-Alancastro, *Polycrystalline Diamond RF MEMS Resonator Technology and Characterization* (Ph.D. Thesis, Dept. of Electrical Engineering, Michigan State University, 2005).

[5] N. Sepulveda, D. M. Aslam, and J. P. Sullivan, submitted to J. MEMS (2006).

[6] P. A. Schultz, K. Leung, and E. B. Stechel, Phys. Rev. B **59**, 733 (1999).

[7] *pictured adapted from website:* http://www.amnh.org/exhibitions/diamonds/structure.html

3.0 Defect-Related Internal Dissipation in ta-C

3.1 Summary

In this section we describe measurements of internal dissipation in tetrahedral amorphous carbon flexural and torsional resonators over the temperature range from 300 to 1023 K. These measurements provide understanding of the defect relaxation processes that occur in this material under oscillatory strain. The mechanical dissipation was found to be controlled by a spectrum of defects within the material, and the magnitude and temperature dependence of the dissipation was found to depend on whether flexural or torsional vibrational modes were excited. The defects that were active under flexural stresses have a relatively flat concentration from 0.4 to 0.7 eV with an ever increasing defect concentration up to 1.9 eV. Under shear stresses (torsion), the defect activation energies increase immediately beginning at 0.4 eV, with increasing defect concentration at higher energies.

3.2 Background

Micro- and nano-electromechanical systems [1,2] (MEMS and NEMS) are being utilized in mass detection [3], force and acceleration sensing [4], and RF applications [5]. Some of these structures are being made from thin films of tetrahedral amorphous carbon (ta-C) [6,7]. Ta-C films are purely amorphous carbon films, with a bond composition of roughly 80% sp^3 and 20% sp^2 [8,9]. Understanding the sources of mechanical dissipation, Q^{-1}, of the MEMS or NEMS structure is tantamount in the performance of the aforementioned applications. As examples, the sensitivity of mass detection and the bandwidth of RF filters and clocks scales as $Q^{1/2}$ and Q^{-1}, respectively [5]. Recently, internal dissipation in ta-C thin films has been investigated, with the conclusion drawn that extrinsic internal dissipation mechanisms dominate dissipative effects [10]. Examples of such mechanisms are structural reconfigurations or atomic motion between equilibrium or metastable states.

In this study, we investigated the temperature dependence of mechanical dissipation in ta-C and related the dissipation to thermally-activated defect relaxation processes. We achieved this by measuring the quality factor (Q) of fixed-free (cantilever) beams and singly clamped torsional oscillators at temperature ranging from 300 to 1023 K and at pressures below 10^{-4} Torr. Following from the previous work, we determined that the Q of the fixed-free beams and the torsional oscillators was not limited by thermoelastic dissipation, phonon-phonon dissipation, clamping losses or air damping [10], even at elevated temperatures. In order to determine the relative defect concentrations, we assume that the strain field associated with the defect couples with the external stress field giving rise to a Debye-like relaxation. This assumption permits us to compare relative defect concentrations with different activation energies. Explicitly, we expect the defects to exhibit a Debye-like relaxation of the following form:

$$Q_{defect} = A\left[\frac{\omega\tau^*}{1+(\omega\tau^*)^2}\right]^{-1}, \qquad (3.1)$$

where A is related to the concentration of the defect and τ^* is the relaxation time for the defect motion. For any given defect, there would be a minimum in Q where $\omega\tau^*=1$. Since we expect the defect relaxation to be thermally activated, the relaxation time would follow an Arrhenius behavior, given by:

$$\frac{1}{\tau^*} = \frac{1}{\tau_0}\exp\left(\frac{-E_A}{k_B T}\right), \tag{3.2}$$

where $1/\tau_0$ is the characteristic atomic vibration frequency, on the order of 10^{13} Hz, E_A is the activation energy for the relaxation process, and k_B is Boltzmann's constant.

3.3 Experiment and Discussion

The ta-C micro-resonators were fabricated using surface micromachining methods as described in Ref. 10. As a brief description, ta-C films were deposited using pulsed-laser deposition (248 nm laser, graphite target, ~ 100 J/cm^2 fluence) on bare Si. The micro-resonators were defined by electron beam lithography in conjunction with aluminum lift-off. The ta-C was etched in an oxygen plasma containing a dilute amount of CF_4. The resonators were released from the substrate by undercutting the silicon below the ta-C using a mixture of dilute HF in HNO_3. Measurements were performed on fixed-free beams (Fig. 3.1a) with lengths 50, 75, 100, 150, 200, and 300 μm and torsional oscillators (Fig. 3.1b) with paddle widths of 15, 17.5 and 20 μm.

Fig. 3.1. Scanning electron micrographs of the oscillator structures. a) Plan view of a fixed-free beam (cantilever). b) Plan view of a torsional oscillator.

The resonant frequencies of the fixed-free beams and torsional oscillators were measured using a laser interference technique [10]. In order to achieve elevated temperatures, the silicon chip with the surface micromachined resonators was attached to a resistive heater element. The oscillators were excited by driving a piezoelectric actuator, separated from the heater element by a porous ceramic thermal isolator. A spectrum analyzer was used to drive the piezoelectric actuator while concurrently measuring the frequency spectra of the voltage from the photodetector. From a least squares Lorentzian fit of the data, we calculated the quality factor, Q, of the devices.

A plot of the quality factor of a 200 μm long fixed-free beam at various temperatures can be seen in Fig. 3.2. A general trend can be seen in the data that as the temperature increases, the quality factor decreases.

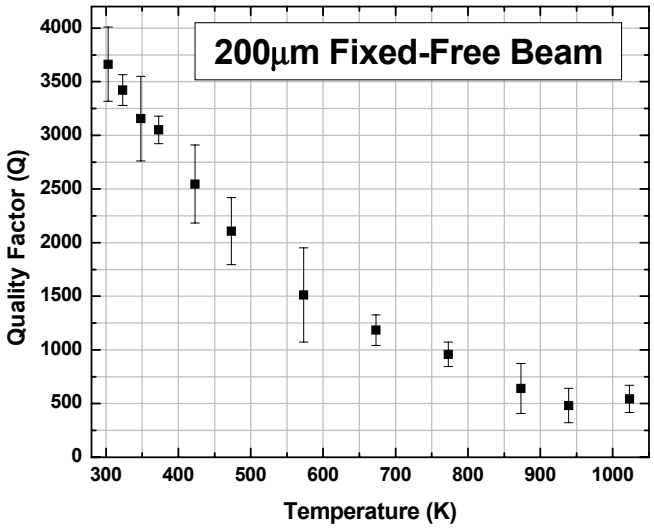

Fig. 3.2. A graph of the Q of a 200 μm long cantilever beam at temperatures ranging from 300 to 1023 K. The Q decreases with increasing temperature for the values measured here.

Following from equations 3.1 and 3.2, the activation energy of the defects can be calculated at the corresponding temperature and frequency for all cantilever lengths. Assuming that Q is proportional to the number of defects and that the nature of the defect relaxation is the same for all defects (i.e. only the activation energy for defect relaxation varies), then we can also determine the relative defect concentration for the oscillators. The defect concentration is normalized by taking the ratio of the inverse Qs at all temperatures by the largest Q (smallest number of defects) for a given oscillator length. A plot of the relative defect concentration versus activation energy for all the cantilever lengths can be seen in Fig 3.3. This shows a relatively flat concentration of defects with energies less than 0.7 eV and an increase in the number of defects with increasing activation energy. From a single plot of concentration versus energy, it is not possible to determine whether the defect spectrum represents a varying distribution of configurationally similar defects having dissimilar activation energies or whether the spectrum represents a distribution of configurationally dissimilar defects. The energy range explored in our study includes the energy needed for interstitial self diffusion in crystalline diamond, 1.3 eV [11], but does not extend to energies required for vacancy self diffusion in crystalline diamond, 2.3 eV [12]. In light of the lower density of ta-C compared to crystalline diamond (about 3.05 g/cm^3 compared to 3.52 g/cm^3), it would be reasonable to expect that a process similar to interstitial self diffusion could be active in ta-C films in this activation energy range. Of course, due to the amorphous nature of ta-C, the distribution of activation energies for self-interstitial diffusion would be expected to be very broad compared to the crystalline material (i.e. no sharp loss peak would be expected).

Using a similar analysis to that used for the fixed-free oscillators, the activation energies and defect concentrations for the torsional oscillators were calculated, a plot of which can be seen in Fig. 3.4. For these oscillators, the defect concentration increases beginning at a lower

activation energy of approximately 0.5 eV compared to the fixed-free beams. The data also suggests that there is a possible maximum in defect concentration at 1.35 eV; however, further experiments at higher temperatures or lower frequencies would need to be performed to confirm this.

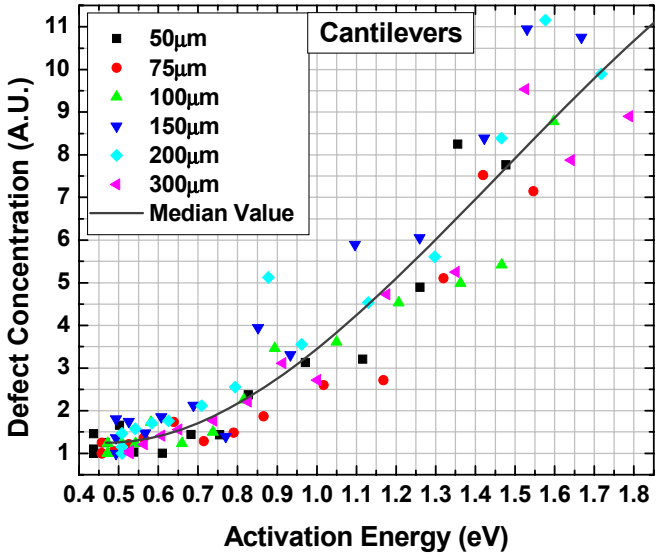

Fig. 3.3. A graph showing the defect concentration for all the cantilever beams versus activation energy. The median value of the concentration for all cantilevers is also plotted. The concentration was determined relative to the oscillator with the highest Q. Each defect was assumed to exhibit a Debye type behavior.

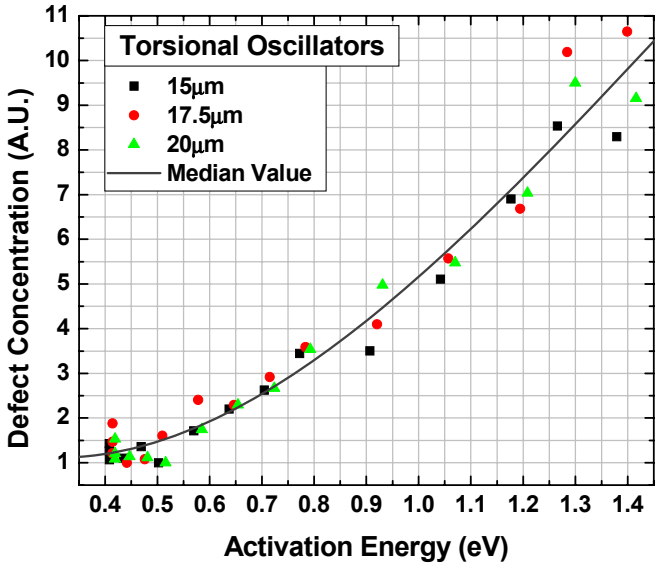

Fig. 3.4. A graph showing the defect concentration for all the torsional oscillators versus activation energy. The median value of the concentration for all torsional oscillators is also plotted. The concentration was determined relative to the oscillator with the highest Q. Each defect was assumed to exhibit a Debye type behavior.

In crystalline systems, it is possible to obtain information regarding the nature of the defects that give rise to mechanical dissipation by comparing the magnitude of dissipation under flexural and torsional stress conditions [13]. We can make a simple estimate of the effect of stress state on the defects that could be present in ta-C assuming a possible defect symmetry. The simplest defect that would give rise to mechanical relaxation in ta-C would be a defect of tetragonal symmetry. This defect would be characterized by a strain tensor of ellipsoidal symmetry with $\lambda_1 \neq \lambda_2 = \lambda_3$ where λ_i is the principal strain along axis i, i.e. the strain tensor has the form,

$$\tilde{\lambda} = \begin{pmatrix} \lambda_1 & 0 & 0 \\ 0 & \lambda_2 & 0 \\ 0 & 0 & \lambda_2 \end{pmatrix} \tag{3.3}$$

This defect symmetry could arise, for example, from the reorientation of an sp^2-bonded (3-fold coordinated) carbon atom. (An sp^2-bonded carbon atom has 3 nearly co-planar sp^2 bonds and an out-of-plane π bond. In this case, $\lambda_1 > \lambda_2$.) Mechanical relaxation (i.e. defect reorientation) of the defect depends on the local stress state experienced by the defect and the defect's orientation with respect to the stress axis. At a sufficiently long time after the application of the stress, the defect relaxation will give rise to a relaxation of the elastic compliance of the material, δJ. Following the formalism of Nowick and Berry [14], the relaxation of the compliance can be estimated for ta-C under flexural (e.g. locally uniaxial) and torsional stress. This estimate is based on the assumption that ta-C is an ideal isotropic solid, the defect has tetragonal symmetry and exists in all possible orientations in the material, and the local stress state is one of either pure uniaxial stress or pure torsion. For the uniaxial stress state, which is relevant for the fixed-free beams, the relaxed compliance is

$$\delta J = \delta E^{-1} \propto C_0 \left[\frac{51}{512} (\lambda_1 - \lambda_2)^2 \right] \tag{3.4}$$

where E is the Young's modulus and C_0 is the total concentration of defects of this type. For the torsional stress state, which is relevant for the torsional oscillators, the relaxed compliance is

$$\delta J = \delta (2G)^{-1} \propto C_0 \left[\frac{41}{512} (\lambda_1 - \lambda_2)^2 \right] \tag{3.5}$$

where G is the shear modulus. Hence, we would expect that the Q for flexural vibrational modes for ta-C to be about 20% lower (dissipation 20% higher) than the Q for torsional vibrational modes. This effect is not clear in our data (not shown), as the resonance frequencies for the torsional oscillators tended to be significantly higher than the resonance frequencies for the flexural oscillators, thus prohibiting a direct comparison at the same measurement frequency.

In this analysis, it is assumed that the same defects are present and operative under flexural and torsional vibrational modes. Since the activation energy for mechanical relaxation of the defect involves some metastable high energy defect configuration that may have high strain

energy, and this strain energy depends on the stress state of the material (uniaxial tension vs. torsion), it is possible that the same defect could exhibit a different activation energy for relaxation under flexural and torsional stresses. A plot that compares the distribution of activation energies determined from the fixed-free and torsional oscillators is shown in Fig. 3.5. The relative defect concentration cannot be compared between these two data sets, only the distributions, so the concentrations have been normalized to permit the curves to overlap and reveal differences in defect distribution. There are subtle, but no large differences in the activation energy distributions between these two data sets with, qualitatively, the largest difference being the shape of the distribution at low activation energies. Since the defect relaxation under flexural or torsional stress states depends only on the difference in principal strains of the defect, $(\lambda_1-\lambda_2)^2$, see Eqs. 3.4 and 3.5, it is not possible to draw any conclusion regarding the exact configuration of the defect that gives rise to dissipation in ta-C.

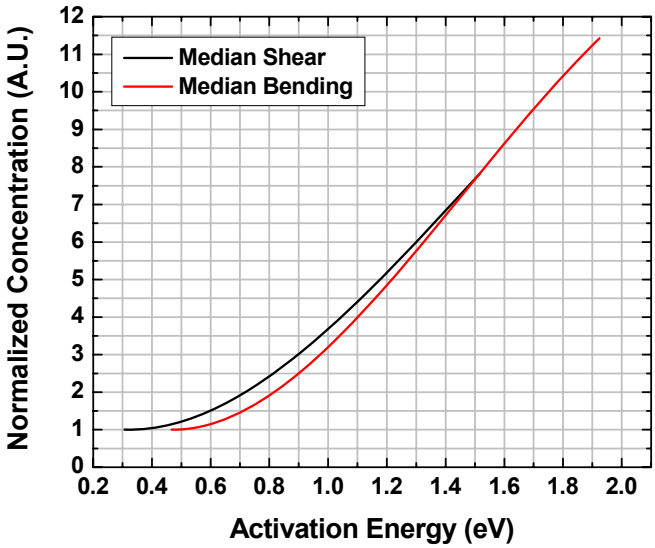

Fig. 3.5. A graph showing the median values of the concentration of defects for both shear and bending stresses versus activation energy. The concentration axis was normalized to permit comparison of the defect distributions.

3.4 Conclusions

In conclusion, we measured the quality factor of fixed-free beams and torsional oscillators with various dimensions over a temperature range of 300 to 1023 K. Assuming the defects that give rise to mechanical dissipation obey a Debye like relaxation and are thermally activated, we calculated the distribution of activation energies for these defects. By normalizing the inverse quality factors, we calculated the relative defect concentrations of the defect spectrum for both flexural and torsional oscillators, and the distributions are similar. No specific defect configuration information can be obtained in this system using the combined data from both the flexural and torsional tests. As a practical point, the sensitivity of mass sensors or the bandwidth of clocks and filters made from fixed-free beams would not diminish for small increases in temperature (up to 200ºC for a 50 μm long beam), but an immediate decrease in sensitivity would be noticeable for devices made from torsional oscillators.

The authors gratefully acknowledge R. Doty for experimental assistance in this work.

3.5 References

[1] K. E. Petersen, Proc. IEEE **70**, 420 (1982).
[2] H.G. Craighead, Science **290**, 1532 (2000).
[3] B. Ilic, et. al, J. Vac. Sci. Technol. **B19**, 2825 (2001).
[4] G. T. A. Kovacs, *Micromachined Transducers Sourcebook* (McGraw-Hill Book Company, New York 1998).
[5] C. T.-C. Nguyen, L. P. B. Katehi, and G. M. Rebeiz, Proc. IEEE **86,** 1756 (1998).
[6] J. P. Sullivan, T. A. Friedmann, and K. Hjort, MRS Bull. **26**, 309 (2001).
[7] D.A.Czaplewski et. al, J. Appl. Phys. **97**, 023517 (2005).
[8] T. M. Alam, T. A. Friedmann, P. A. Schultz, and D. Sebastiani, Phys. Rev. B **67**, 245309 (2003).
[9] P.A. Schultz, K. Leung, and E. B. Stechel, Phys. Rev. B **60**, 1551 (1999).
[10] D.A. Czaplewski, J.P. Sullivan, T.A. Friedmann, D.W. Carr, B.E.N. Keeler, and J.R. Wendt, J. Appl. Phys. **97**, 023517 (2005).
[11] J. F. Prins, Phys. Rev. B **44**, 2470 (1991).
[12] G. Davies, S. C. Lawson, A. T. Collins, A. Mainwood, S. J. Sharp, Phys. Rev. B **46**, 13157 (1992).
[13] B. S. Berry, Acta Met. **9**, 98 (1961).
[14] A. S. Nowick and B. S. Berry, *Anelastic Relaxation in Crystalline Solids, Ch. 8.* (Academic Press, Inc., New York, 1972).

4.0 Temperature-Dependent Mechanical Behavior of ta-C

4.1 Summary

The complete elastic properties of tetrahedrally-coordinated amorphous carbon (ta-C) thin films have been measured in the temperature range 300 K to 873 K. Flexural and torsional mechanical oscillators were fabricated from ta-C, and using the resonant frequency of the oscillators as a function of temperature, we calculated the temperature-dependent Young's and shear moduli (658 ± 24 GPa and 271 ± 6.6 GPa, at 300 K, respectively). From these values, we calculated the bulk modulus, Poisson's ratio and the elastic stiffness and compliance constants as a function of temperature. In addition, the temperature dependence of the coefficient of thermal expansion of ta-C was determined using a wafer curvature technique.

4.2 Introduction and Background

Micro- and Nano-Electromechanical Systems [1,2] (MEMS and NEMS) are being used in ever increasing applications, such as high sensitivity sensors of mass [3] and acceleration [4], filters for high frequency electrical signals, clocks, etc.[5] Recently, MEMS structures have been fabricated from thin films of tetrahedral amorphous carbon (ta-C), also known as amorphous diamond.[6,7] This material consists of a mixture of sp^3-bonded and sp^2-bonded carbon where the sp^3 component is the majority component (about 80%), comprising the matrix phase, and the sp^2 component (about 20%) forms low dimensional clusters within this matrix.[8,9] The room temperature mechanical properties of this material have been previously reported based on MEMS tensile test structures, surface Brillouin scattering, and nanoindentation.[10,11,12,13] In this letter, we report the first measurements of the temperature dependent mechanical properties of this material. These results can be used to predict the thermal drift of ta-C MEMS or NEMS resonators when operating at elevated temperatures.

4.3 Experiment and Discussion

In this study, we fabricated MEMS flexural and torsional oscillators out of ta-C and used these structures to extract the Young's, E, and shear, G, moduli at temperatures ranging from 300 K to 873 K. Due to the isotropic nature of this material, there are only two independent elastic constants, from which the other mechanical constants can be calculated, including the elastic stiffness constants, C_{11}, C_{12}, and C_{44}, Poisson's ratio, ν, bulk modulus, B, and elastic compliance constants, S_{11}, S_{12}, and S_{44}. We report both the values at 300 K and polynomial fits to the temperature-dependent properties over the range 300 K to 873 K.

The surface micromachined MEMS flexural oscillators were fabricated in a similar process to those reported earlier.[7] The oscillators were defined using electron-beam lithography, and the dimensions of several oscillators were quantified using scanning electron microscopy (SEM). To extract the Young's modulus, we fabricated flexural oscillators with a range of lengths, l, of 50, 75, 100, 150, 200, and 300 μm and a fixed thickness, t, and width, w (Fig. 1a). An SEM image of a 50 μm long oscillator can be seen in Fig. 1b. We also fabricated singly-clamped torsional oscillators in order to extract the shear modulus. These oscillators had a thickness, t, paddle length, p, beam length, l, support beam width, b, and paddle widths, w, of 15, 17.5 and 20 μm (Fig. 1c). An SEM image of a torsional oscillator with a paddle width of 20 μm

can be seen in Fig 1d. The lowest resonant frequencies of the flexural and torsional oscillators are given by:

$$f = \frac{(1.875)^2}{2\pi}\frac{t}{l^2}\sqrt{\frac{E}{12\rho}} \text{ and } f = \sqrt{\frac{0.0429 G b^3}{\rho p l w^3}}, \quad (4.1)$$

respectively, where E, G and ρ are the Young's modulus, shear modulus, and density of the ta-C film, respectively.

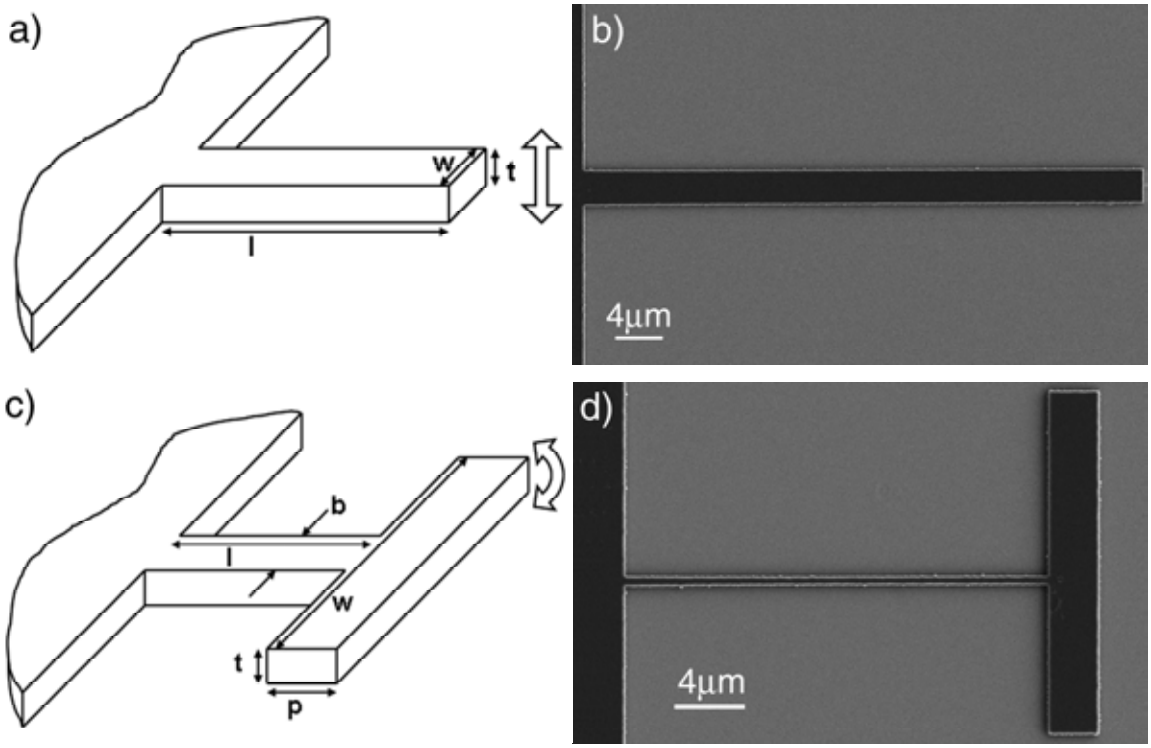

Fig. 4.1. a) Schematic of a flexural oscillator used to determine the Young's modulus of the ta-C film. b) Scanning electron micrograph (SEM) of a flexural oscillator. c) Schematic of a torsional oscillator used to determine the shear modulus of the ta-c film. d) SEM of a torsional oscillator.

The resonant frequencies of the oscillators were measured using a laser interference method, similar to an earlier reported method.[7] For temperature-dependent studies, the silicon chip with the oscillators was mounted onto the face of a resistive heater element. A thermocouple was epoxied to the top of the silicon chip to measure its temperature, and a piezoelectric transducer, which provided mechanical actuation of the oscillators, was epoxied to the back of the heater with a porous ceramic thermal isolator in between. The entire assembly was placed in a vacuum chamber and evacuated to 10^{-5} Torr. A spectrum analyzer was used to drive the piezo-element while simultaneously measuring the output from a photodetector. The spectra were swept over a frequency window, and the resonant frequency was obtained by a Lorentzian fit to the square of the voltage from the photodetector. For a given length, six different flexural oscillators were measured at every temperature, and the Young's modulus at each temperature was determined by a least squares fit to the frequency versus l^{-2} curve. In a similar fashion, for each given paddle width, 5 torsional oscillators were measured. Their resonant frequencies were

plotted versus $w^{-3/2}$, and the shear modulus at each temperature was determined by a least squares fit. The moduli were extracted at various temperatures up to 873 K.

Plots of the Young's and shear moduli as a function of temperature are shown in Figs. 4.2a and 4.2b, respectively. After calculating both E and G at each temperature, we used the following relationships to calculate the other properties of the ta-C film:

$$\upsilon = \frac{E}{2G} - 1, \text{ and } B = \frac{E}{3(1-2\upsilon)} \tag{4.2}$$

$$C_{11} = \frac{G(4G-E)}{(3G-E)},\ C_{12} = \frac{G(E-2G)}{(3G-E)}, \text{ and } C_{44} = G, \tag{4.3}$$

$$S_{11} = \frac{C_{11}+C_{12}}{(C_{11}-C_{12})(C_{11}+2C_{12})},\ S_{12} = \frac{-C_{12}}{(C_{11}-C_{12})(C_{11}+2C_{12})}, \text{ and } S_{44} = \frac{1}{C_{44}}. \tag{4.4}$$

We then performed a least squares fit of all the elastic constants and mechanical properties to a second order temperature dependent polynomial of the following form:

$$y = \sum_{n=0}^{2} A_n (T-300)^n, \tag{4.5}$$

where A_n are the fitting parameters, and T is the temperature in Kelvin, with A_o being the fit of the room temperature value. Fits of the Young's and shear moduli are the solid lines in Figs 4.2a and 4.2b. The values obtained for each property of the ta-C film can be found in Table 4.1.

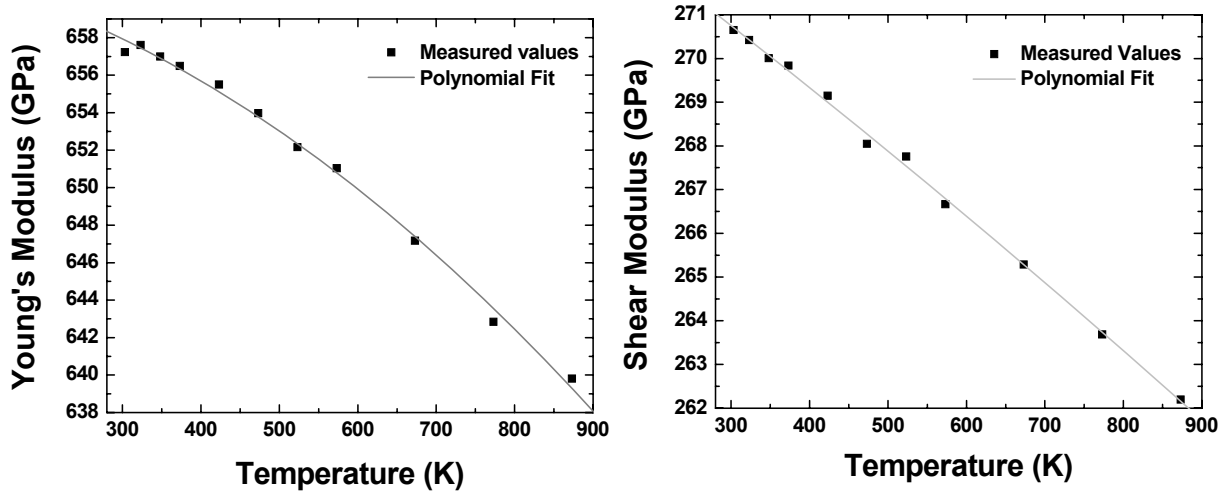

Fig. 4.2. a) Graph of the Young's modulus measured at various temperatures. b) Graph of the shear modulus measured at various temperatures. Also shown is the least squares polynomial regression for both data sets. Included in the plots are the data points corrected for the room temperature shift in modulus.

The moduli show a monotonic decrease at elevated temperatures. Calculated from the measured values of the two moduli, the elastic constant, C_{11}, also shows a decrease with temperature. The decrease (~2%) with increasing temperature is similar to the one seen in the

value of C_{11} for crystalline diamond.[14] This might be expected due to the large fraction of sp^3 bonding in the material (80%).

Table 4.1. Temperature dependence of the mechanical properties of the ta-C film. $Y=\Sigma A_n(T-300)^n$. *The A_0 value is the fit of the data at room temperature.*

	A_0	A_1	A_2
E	662 ± 24 GPa	-7.6 ± 5.3 MPa/K	-21 ± 5 kPa/K^2
G	275 ± 7 GPa	-13.0 ± 1.7 MPa/K	-2 ± 1 kPa/K^2
B	368 ± 38 GPa	71.9 ± 25.2 MPa/K	-68 ± 22 kPa/K^2
C_{11}	739 ± 80 GPa	39.3 ± 18.0 MPa/K	-58 ± 16 kPa/K^2
C_{12}	190 ± 5 GPa	65.4 ± 19.6 MPa/K	-55 ± 17 kPa/K^2
C_{44}	275 ± 7 GPa	-13.0 ± 1.7 MPa/K	-2 ± 1 kPa/K^2
S_{11}	1.51x10^{-12} ± 6x10^{-14} Pa^{-1}	1.4x10^{-17} ± 1.2x10^{-17} Pa^{-1}K^{-1}	5.3x10^{-20} ± 1.1x10^{-20} Pa^{-1}K^{-2}
S_{12}	-3.1x10^{-13} ± 7x10^{-14} Pa^{-1}	-7.1x10^{-17} ± 1.7x10^{-17} Pa^{-1}K^{-1}	3.6x10^{-20} ± 1.4x10^{-20} Pa^{-1}K^{-2}
S_{44}	3.64x10^{-12} ± 9x10^{-14} Pa^{-1}	1.70x10^{-16} ± 2.4x10^{-17} Pa^{-1}K^{-1}	3.5x10^{-20} ± 2.1x10^{-20} Pa^{-1}K^{-2}
ν	0.202 ± 0.054	5.38x10^{-5} ± 1.6x10^{-6}	-3.9x10^{-8} ± 1x10^{-9}

The errors associated with the values of parameter *A* were calculated from error analysis, using the following values and their uncertainty. For both oscillators, *t* was measured to be 560 ± 5 nm using an SEM, and a value of ρ of 3.050 ± 0.100 g/cm^3 was used. Additionally, in calculating the uncertainty of *E*, the uncertainty in *l* was accounted for in the least squares fit of resonant frequency versus l^{-2}. In the calculation of the uncertainty in *G*, *p* was measured to be 3000 ± 10 nm, *b* was measured to be 560 ± 5nm, and the uncertainty in *l* was calculated not to contribute significantly. The uncertainty in the density was the largest contributor to the uncertainty in *E*. The density was calculated from the measured sp^3 content [8] and using reference [15], also from x-ray reflectivity.[16] The largest uncertainty in *G* arose from the uncertainty in the thickness of the film, *t*, and the width of the torsional support, *b*. The uncertainty in the values of *E* and *G* were used to obtain the uncertainties in the other values using error analysis. The uncertainty of temperature coefficients, A_1 and A_2, are listed in Table 3. The thermal expansion coefficient, α, was determined separately from the mechanical properties through measurements of the curvature of a thin ta-C film on a silicon substrate at elevated temperatures and the use of Stoney's equation [17] with the temperature-dependent moduli for ta-C that was determined here and literature values for the temperature-dependent properties of Si.[18] A third order polynomial of the form of Eq. (4.5) was needed to accurately fit the temperature dependent behavior of α.

4.4 Conclusions

In conclusion, we have performed the first measurements of the temperature-dependent mechanical properties of ta-C films. Flexural and torsional MEMS oscillators were fabricated out of ta-C, and the resonant frequencies were measured in the temperature range of 300 K to 873 K. At room temperature, the Young's modulus, shear modulus, and Poisson's ratio were found to be 662 ± 24 GPa, 275 ± 7 GPa and 0.202 ± 0.054, respectively. We also measured the temperature dependent behavior of the thermal expansion coefficient of ta-C, and a room temperature value of $1.47 \times 10^{-6} \pm 2.5 \times 10^{-7}$ was observed.

The authors gratefully acknowledge R. Doty and B. McKenzie for experimental assistance.

4.5 References

[1] K. E. Petersen, Proc. IEEE **70**, 420 (1982).
[2] H.G. Craighead, Science **290**, 1532 (2000).
[3] B. Ilic, et. al, J. Vac. Sci. Technol. **B19**, 2825 (2001).
[4] G. T. A. Kovacs, *Micromachined Transducers Sourcebook* (McGraw-Hill Book Company, New York 1998).
[5] C. T.-C. Nguyen, L. P. B. Katehi, and G. M. Rebeiz, Proc. IEEE **86,** 1756 (1998).
[6] J. P. Sullivan, T. A. Friedmann, and K. Hjort, MRS Bull. **26**, 309 (2001).
[7] D.A.Czaplewski et. al, J. Appl. Phys. **97**, 023517 (2005).
[8] T. M. Alam, T. A. Friedmann, P. A. Schultz, and D. Sebastiani, Phys. Rev. B **67**, 245309 (2003).
[9] P.A. Schultz, K. Leung, and E. B. Stechel, Phys. Rev. B **60**, 1551 (1999).
[10] D. A. LaVan, R. J. Hohlfelder, J. P. Sullivan, T. A. Friedmann, M. Mitchell, C. I. H. Ashby, Mater. Res. Soc. Proc. **594**, 295 (2000).
[11] S. Cho, I. Chasiotis, T. A. Friedmann, and J. P. Sullivan, J. Micromech. Microeng. **15**, 728 (2005).
[12] A. C. Ferrari, J. Robertson, M. G. Beghi, C. E. Bottani, R. Ferulano, and R. Pastorelli, Appl. Phys. Lett. **75**, 1893 (1999).
[13] T. A. Friedmann, J. P. Sullivan, J. A. Knapp, D. R. Tallant, D. M. Follstaedt, D. L. Medlin, and P. B. Mirkarimi, Appl. Phys. Lett. **71**, 3820 (1997).
[14] E.S. Zouboulis, M. Grimsditch, A. K. Ramdas, and S. Rodriguez, Phys. Rev. B, **57**, 2889 (1998).
[15] A. C. Ferrari, B. Kleinsorge, G. Adamopoulos, J. Robertson, W. I. Milne, V. Stolojan, L. M. Brown, A. LiBassi, and B. K. Tanner, J. Non-Cryst. Sol, **266-269**, 765 (2000).
[16] M. P. Siegal, D. R. Tallant, P. N. Provencio, D. L. Overmyer, R. L. Simpson, and L. J. Martinez-Miranda, Appl. Phys. Lett. **76**, 3052 (2000).
[17] G.G. Stoney, Proc. R. Soc. London **9**, 172 (1909).
[18] C.A. Swenson, J. Phys. Chem. Ref. Data **12**, 179 (1983).

5.0 Defect-Related Internal Dissipation in Polycrystalline Diamond

5.1 Summary

In the prior sections, we described the mechanical behavior and defect-related internal dissipation in amorphous carbon thin films. This material has a broad spectrum of defect relaxation processes, leading to appreciable mechanical dissipation over a large temperature range. In order to contrast the mechanical relaxation of an amorphous material to a crystalline material, a study of dissipation and temperature mechanical behavior was performed using crystalline diamond thin films. Boron doped ($5x10^{19}$ cm^{-3}) and undoped polycrystalline diamond (poly-C) films with a thickness of approximately 0.7 μm, grown at 600 °C or 780 °C, were used to fabricate cantilever-beam resonators with dimensions in the range of 0.1 – 100 μm. These structures were studied in the temperature range of 23 - 400 ºC. Very high quality factors are observed in this material, up to 116,000, in comparison to amorphous carbon resonators (Q of about 4000). We also measured the temperature coefficient of resonance frequency in this material, and it was in the range of -1.59×10^{-5} to -2.56×10^{-5} $°C^{-1}$, which is mainly related to changes in the Young's modulus with temperature. In contrast to amorphous carbon, which showed monotonic increases in internal dissipation with temperature, an apparent peak in the dissipation is observed for the highly-doped poly-C film, suggesting the dominance of a single defect type.

5.2 Background and Introduction

As the performance of a microresonator is characterized by its resonant frequency and quality factor (Q), a number of recent studies have focused on increasing the resonance frequencies and Qs of poly-Si microresonators. For most applications, a GHz frequency range and a Q of at least 10,000 is required. While the miniaturization of poly-Si resonators has been used to achieve a resonance frequency of 1.169 GHz, the measured Q of 5,846 reported for this frequency [1] is substantially lower than the desired value. In other studies, the elimination of anchor losses by placing the anchors at the nodes [2], the removal of surface contamination or defects [3][4] and the elimination of thermoelastic dissipation (TED) by using torsional microresonators [5] have been investigated to increase the Q. However, for most polycrystalline materials the Q is limited by intrinsic mechanisms that involve thermally activated relaxation processes [6][7][8]. These mechanisms are usually related to grain boundary sliding or internal friction, phonon-phonon interaction or defects within the resonator material [7]. However, for polycrystalline diamond (poly-C), some of these mechanisms (grain boundary sliding for example) may not be applicable due to very low diffusion coefficients of most atoms in poly-C.

Poly-C has been recently investigated for its possible use in MEMS packaging [9][10], BioMEMS [11] and RFMEMS [12][13][14][15]. It has been reported that temperature fluctuations can affect adversely the frequency and Q of microresonators made of nickel [3][4], poly-Si [16][17], nanocrystalline diamond [18][19] and polycrystalline silicon carbide (poly-SiC) [20]. Although a Q of 55,000 and a resonance frequency of 1.5 GHz have been reported for disc resonators made from nanocrystalline diamond [21], the thermal stability of poly-C resonators and the factors that cause Q degradation in such devices are not well understood.

In order to study the temperature dependence of frequency and Q in poly-C microresonators, the main focus of this section is to (i) understand their intrinsic dissipation

mechanisms responsible for limiting the highest achievable Q and (ii) find their frequency shifts when tested at elevated temperatures.

5.3 Experimental

The cantilever-beam poly-C μresonators used in this study have lengths, thicknesses and widths in the ranges of 100 – 500 μm, 0.6 - 0.7 μm and 10 μm, respectively, and were fabricated using undoped and p-type poly-C films. The poly-C nanoresonators have lengths, thicknesses and widths in the ranges of 40 – 200 μm, 0.7 μm and 0.1 – 0.5 μm, respectively.

As shown in Fig. 5.1, the fabrication process starts with an n-type (100) Si wafer coated with a 2 μm SiO_2 layer. The SiO_2 layer, used as the sacrificial layer, is patterned to create the anchor holes for the poly-C cantilevers. For poly-C growth on Si in the anchor area and on SiO_2 in other areas, the seeding technique consists of the use of a diamond powder loaded water suspension, called DW [22], which is prepared by mixing 25 carats of diamond powder, with an average particle size of 25 nm, in 1000 ml of de-ionized water and a suspension reagent. The beaker with DW suspension is placed in an ultrasonic bath for 30 minutes before it is applied to the sample surface. A 30 sec HF etch removed any surface contamination and improved the overall surface coverage of the sample as the pure SiO_2 surface is hydrophilic (although the anchor areas are hydrophobic, the etch was found to be useful). The DW seeding is accomplished in a conventional spinner for 30 seconds at 1000 rpm. For improving the seeding density, the spinning process was repeated 2 times to achieve a nucleation density of 1×10^{11} cm^{-2} [12]. After the seeding step, the samples were loaded into a microwave plasma CVD (MPCVD) reactor for poly-C growth.

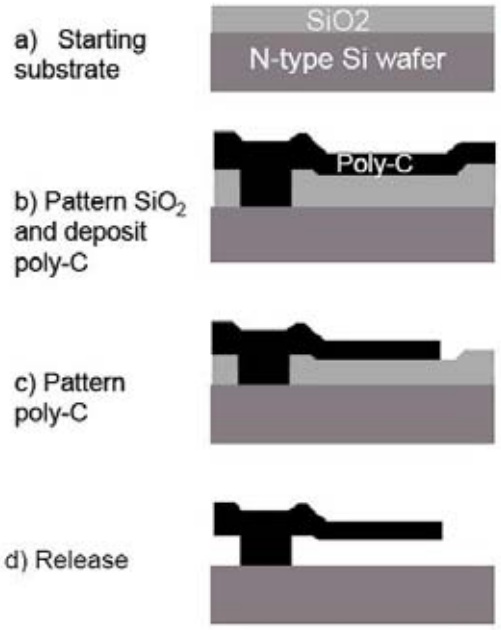

Fig. 5.1. Process flow for the fabrication of poly-C micro and nanoresonators.

In order to have a broad characterization of poly-C microresonators, three samples were fabricated. "Sample 1" has an undoped 0.6 μm thick poly-C film grown at 780 °C and "sample 2" has a highly B-doped ($5x10^{19}$ cm^{-3}) [22] 0.7 μm thick poly-C film grown at 780 °C. "Sample

3" has an undoped 0.7 µm thick poly-C film grown at 600 °C. Each sample represents one specific type of polycrystalline diamond film from which different cantilever structures were fabricated and tested. The poly-C film growth parameters for all the samples are shown in Table 5.1. The doping was done *in-situ* using tri-methyl-boron (TMB) diluted in hydrogen (0.098%) as the source for boron. The growth temperatures were monitored by a pyrometer, and temperature fluctuation was kept below +/- 5°C. Fig 5.2 shows the Raman spectra for the three different poly-C films, where the sharpest diamond (sp^3 carbon-carbon bonding) peak at 1332 cm^{-1} can be observed for sample 1. This is because the higher growth temperatures lead to higher sp^3/sp^2 ratios. It may also be noted that the lower Raman peak of sample 2 is due to the high level of doping, which is known to decrease the sp^3/sp^2 ratios in poly-C films [23].

Table 5.1. Parameters used for poly-C growth and patterning. The superscript represents the sample on which the value was used.

Poly-C Film Growth		
Gas Flow Rate (sccm)	**H_2**	**$100^{1,2,3}$**
	CH_4	**$1^{1,2,3}$**
	TMB	**4^2 ; $0^{1,3}$**
Temperature (ºC)		**$780^{1,2}$; 600^3**
Microwave Plasma Power (kW)		**$2.0^{1,2,3}$**
MPCVD Gas Pressure (torr)		**$35^{1,2,3}$**
Seeding Diamond Powder Size (nm)		**$25^{1,2,3}$**
Dry Etching Parameters		
Gas Flow Rate (sccm)	**CF_4**	**$1^{1,2,3}$**
	O_2	**$30^{1,2,3}$**
Chamber pressure (mbar)		**$4x10^{-2}$ ^{1,2,3}**
DC Power (W)		**400 ^{1,2,3}**

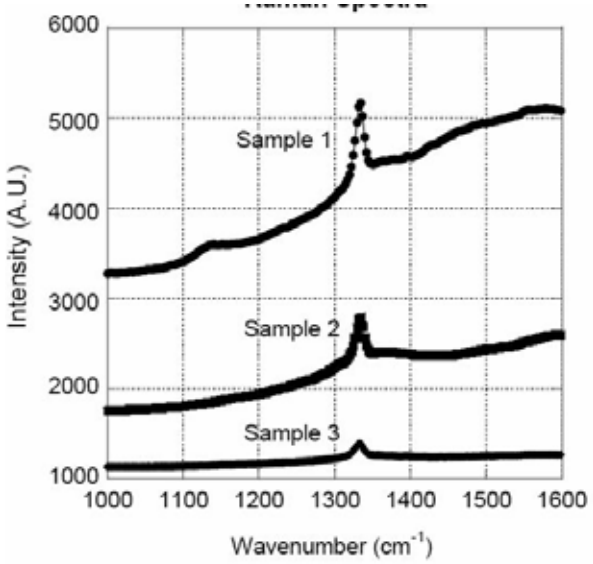

Fig. 5.2. Raman spectra for the three studied poly-C samples.

The patterning of the poly-C cantilevers was done by using an RF dry etching system and using the parameters shown in Table 5.1. The etch rate for samples 2 and 3 were about to 0.04 μm/minute, and 0.02 μm/minute for the sample 1. Following the release of poly-C resonators by etching the samples in HF for 50 minutes, the cantilevers remained flat with less than approximately 1 μm out-of-plane curvature over the length of the beam, even for the longest beams. This indicates that there is little strain gradient in the films. In the past, this fabrication process has been used to produce beams that were fixed on both ends (a bridge structure) and they did not show buckling, which is an indication that the films were not under a state of high net compressive stress prior to release [12]. The fabrication technology developed in this work is capable of producing clean and smooth poly-C structures with a minimum feature size of 2 μm as shown in Fig. 5.3 (the combdrives with over 100 micrometer spring beams support the fact that our technology leads low stress films for different types of resonator structures).

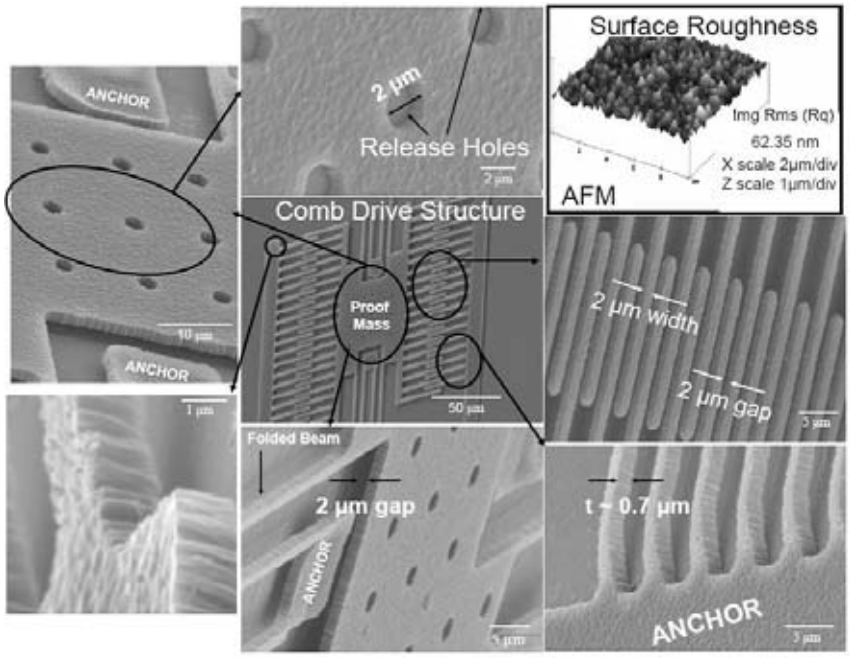

Fig. 5.3. Poly-C comb-drive structures produced using the described fabrication process flow and dry etching technique. The AFM image is a representative sample of the poly-C film surface.

Right after the cantilevers were released, they were taken in a ultra-violet (UV) ozone system for cleaning, and then heated to 800 ºC for 1 minute in an argon atmosphere using rapid thermal annealing to remove any moisture. Before every measurement, the samples were cleaned using this procedure, which led to a reproducible sample condition.

The poly-C nanoresonators were fabricated as cantilever beams with lengths and widths in the ranges of 40 – 150 μm and 100 nm – 500 nm, respectively. All the nanoresonators were fabricated from sample 1. Electron beam (e-beam) lithography has been used in the past to fabricate single crystal silicon nanoresonators [5][24][25]. This same technique is used in this work to pattern poly-C. E-beam lithography was used to define an aluminum etch mask layer on top of the poly-C film. The nanocantilevers were defined using an oxygen plasma dry etch followed by a wet etch of the underlying sacrificial SiO_2 layer. Minimum feature sizes of 100 nm were defined in poly-C films with thickness of 0.6 *μm*, even though the poly-C films had an

RMS roughness of about 60 nm as can be seen in the AFM inset in Fig. 5.3. The fabrication of poly-C nanoresonators indicates that free-standing structures down to the nano-scale can be defined in polycrystalline diamond films even with notable film roughness. A detailed study of nanoresonators will be the subject of a subsequent publication.

Fig. 5.4 shows the testing set up and SEM images of some of tested poly-C cantilevers with their dimensions. All measurements were made at a vacuum level below 1×10^{-5} Torr in order to eliminate air damping losses. The actuation of the beams was done by using a spectrum analyzer to drive a piezo transducer element that was physically attached to a ceramic cylinder. The end of the ceramic cylinder that is not in contact with the piezo was fixed to a current controlled heater, and the sample is placed on the other end of the heater. The temperature on the sample was controlled by this heater, which kept the set temperature within 1% of the set value.

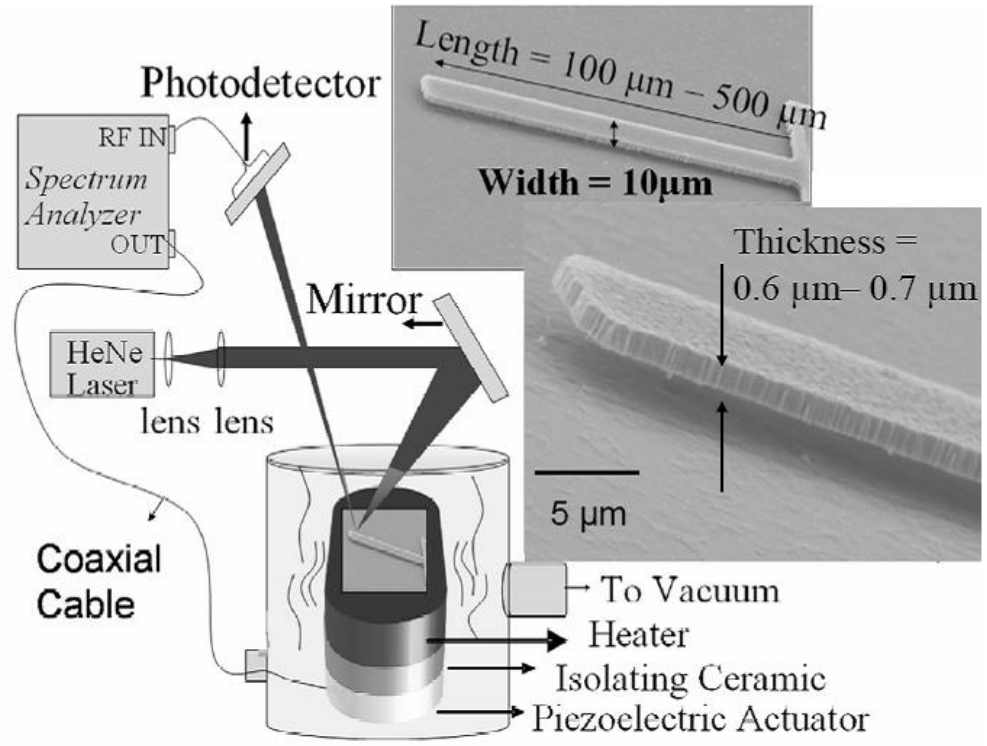

Fig. 5.4. Testing set-up for measurements using piezoelectric actuation and laser detection. The actual test geometry employed interferometric detection (the light reflecting off the sample interferes with the incident light). Inset SEM image shows poly-C cantilevers with their dimensions.

The detection was done by focusing a laser beam onto the end of the vibrating cantilever. The light reflecting off of the sample interferes with the incident light, and this interference leads to modulation of the light leaving the sample surface. Some of this light is sent to a photodetector, where the AC frequency on the photodetector represents the frequency of vibration of the structure. This frequency is determined by a spectrum analyzer connected to the photodiode output.

5.4 Results and Discussion

The frequency and Q values of poly-C μresonators were obtained from Lorentzian fits [26] to the measured data. The resonant frequency of a cantilever beam depends on the Young's modulus according to the following equation [7][27]:

$$f_0 = \frac{c^2 t}{2\pi l^2}\sqrt{\frac{E}{12\rho}} \quad , \tag{5.1}$$

where E is Young's modulus, ρ is the density of the cantilever material; *t* and *l* are the cantilever beam thickness and length, respectively, and *c* is a constant that depends on the cantilever vibration mode, which for the first vibration mode of cantilever equals 1.875 [27]. The elastic properties of poly-C vary with temperature [28] and consequently so does the poly-C Young's modulus. The Young's modulus of poly-Si has been reported to decrease about 8% of its value at room temperature in the temperature range of 23 - 250 ºC [29], while the Young's modulus for poly-C has been reported to decrease about 3% of its value at room temperature in the temperature range of 23 - 400 ºC [28][30]. According to (1), a shift in the Young's modulus will result in a shift of the resonant frequency if temperature dependence of other parameters is neglected. The shifts in the resonant frequency of a microresonator due to changes in temperatures are quantified by the temperature coefficient of resonant frequency (TC_f) [2]:

$$TC_f = \frac{f_T - f_o}{f_0 \times (T - To)} \quad , \tag{5.2}$$

where f_0 and f_T are resonant frequencies at temperatures of 300 K and T, respectively, and and T_o is room temperature.

Figs. 5.5, 5.6 and 5.7 show the frequency shift as a function of measurement temperature for 300 μm and 400 μm long cantilever beams. The TC_f values were obtained by calculating the slopes of linear fits done to the measured data. It may be pointed out that due to a smaller number of data points, the computed TC_f values are approximate. Table 5.2 shows a summary of the results obtained for poly-Si by other research groups and the results obtained for poly-C reported in this work. Results on the TC_f values for poly-Si structures at temperatures above 247 ºC have not been reported. For comparison purposes, the TC_f values for poly-C resonators reported in this work ranged from -1.37×10^{-6} to -2.74×10^{-6} in the temperature range of 23 ºC – 100 ºC and from -1.15×10^{-5} to -2.31×10^{-5} in the temperature range of 23 ºC – 250 ºC. These values show that poly-C μresonators have TC_f values similar to those obtained for poly-Si bridges and free-free beams [2], and to those obtained from geometrically compensated poly-Si structures [16][17].

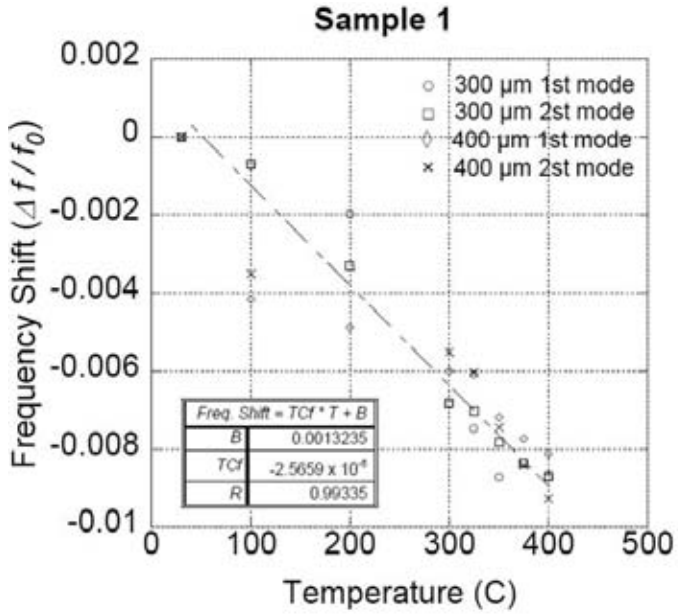

Fig. 5.5. Frequency shift with temperature for sample 1 and linear fit to the measured data.

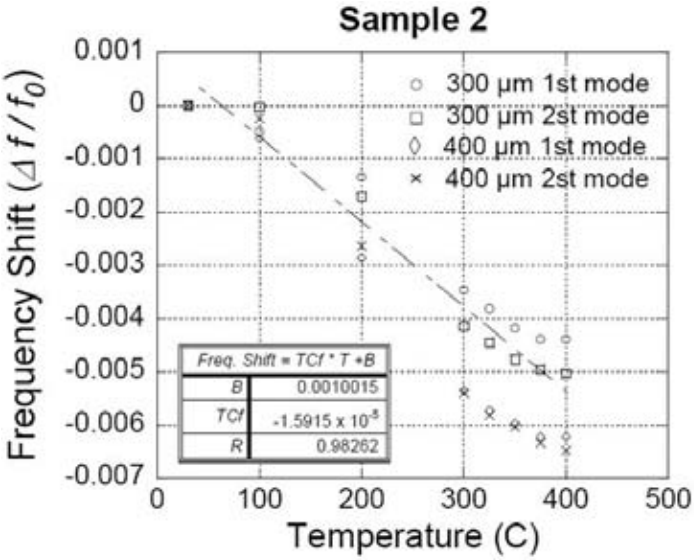

Fig. 5.6. Frequency shift with temperature for sample 2 and linear fit to the measured data.

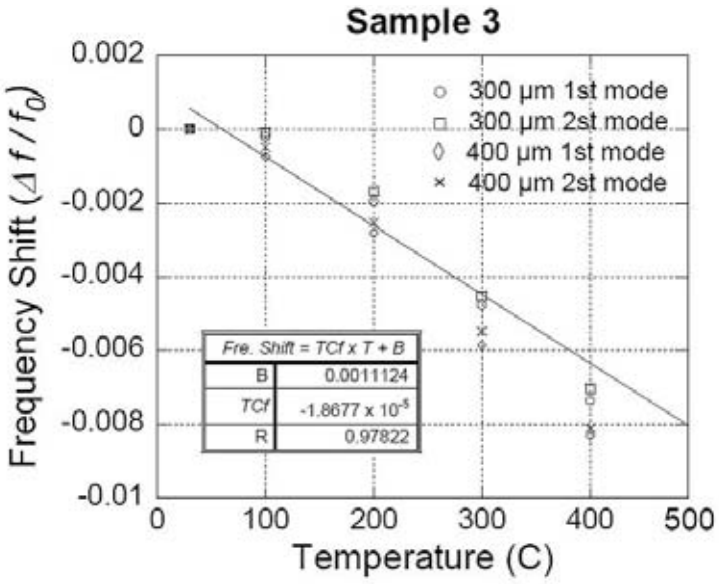

Fig. 5.7. Frequency shift with temperature for sample 3 and linear fit to the measured data.

Table 5.2. Temperature dependent frequency performance for poly-Si and the poly-C µresonators reported in this work.

Poly-Si				
Structure	$\Delta f / fo\,(ppm)$	Temperature Range (°C)	TC_f (ppm/°C-1)	Resonant Frequency (*fo*) Range
Free-Free Beam [8]	≈ - 1000	30 – 247	-12.5	53.6 MHz
Clamped-Clamped [8]	≈ - 3600	30 – 247	-16.7	4.2 MHz
Comb-Drive [33]	≈ - 1200	30 – 107	-15.6	≈ 345 KHz
Comb-Drive (Compensated) [33]	≈ - 600	30 – 107	-7.8	≈ 345 KHz
Clamped-Clamped (Compensated) [14];[15]	≈ - 240 ; ≈ - 18	30 – 107	-2.5 ; -0.24	≈ 10 MHz
Poly-C (cantilever beams reported in this work)				
Sample 1	≈ - 8,450	30 – 400	≈ -25.6	12 KHz – 50 KHz
Sample 2	≈ - 5,900	30- 400	≈ -15.9	8 KHz – 31 KHz
Sample 3	≈ - 6,100	30 – 400	≈ -18.6	8 KHz – 15 KHz

If the poly-C density is assumed to be (3520 kg-m^{-3}), the temperature dependence of the poly-C Young's modulus can be calculated from the measured frequency shifts and using equation (1). Fig. 5.8 shows the resulting Young's modulus values. In the temperature range of 23– 400 ºC, the samples showed a Young's modulus decrease of 2.5% for sample 1, 3.8% for sample 2 and 2.6% for sample 3. The room temperature Young's modulus varies from sample to sample, showing the highest value of 990 GPa for sample 1.

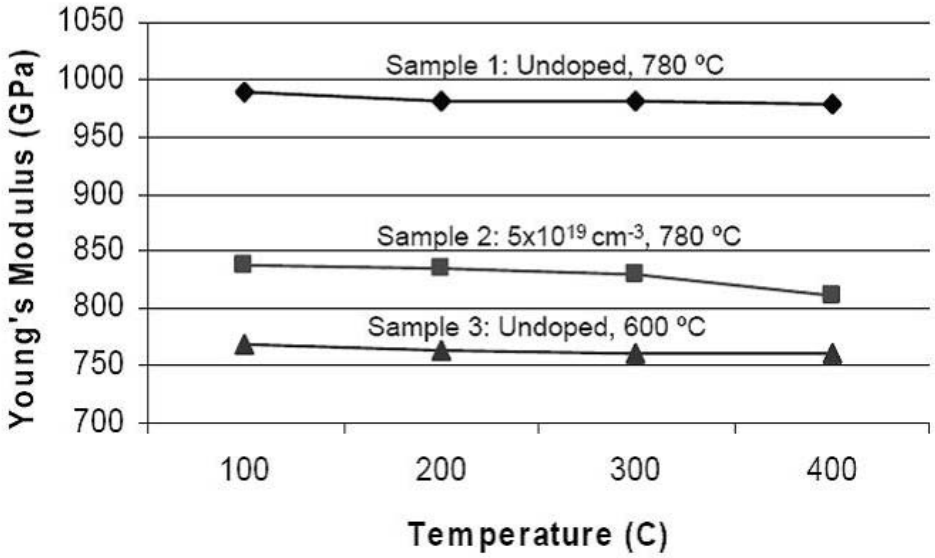

Fig. 5.8. Poly-C Young's modulus temperature dependence for the three studied samples.

Fig. 5.9 shows a plot of the measured Q values as a function of frequency and the resonant peak with the highest Q value for each sample. The measured Q values for the cantilevers made from sample 1 are about 2 times larger than those for the other two poly-C films. The highest Q value of 116,000 that has been measured so far for any polycrystalline diamond structure or a cantilever made of any polycrystalline material was measured on the sample 1. This value is also much larger than nanocrystalline diamond resonators reported in the past [18][19][21] and is about half the value of 250,000 found for single crystal silicon resonators [25].

Fig. 5.10 shows the distribution of measured Q values for the three poly-C samples along with the measured distribution of grain sizes. The majority of the measured Q values from sample 2 are between 8,000 and 40,000, and the majority of the measured Q values on sample 3 are between 4,000 and 25,000. However, sample 1 shows a much higher maximum Q and a larger variation in measured Q values, with the majority of the measured Q values between 4,000 and 100,000. The Q of a resonator may be controlled by a variety of loss mechanisms, some of which are intrinsic to the material, some of which are controlled by the mechanical design of the resonator, and some of which are due to extrinsic effects, such as surface contamination. Resonators with high Q are especially sensitive to surface cleanliness, as dust or other particles that might be attached to the resonator surface during processing may lower the Q from its intrinsic value. The large variation in Q for sample 1 might reflect the effect of processing-induced defects. In that case, the highest Q's for the samples should be the most indicative of the intrinsic Q of the material. In order to deduce what dissipation mechanisms might be operative in poly-C resonators it is useful to compare the Q's of these resonators with the predicted Q's assuming intrinsic and design-related dissipation mechanisms.

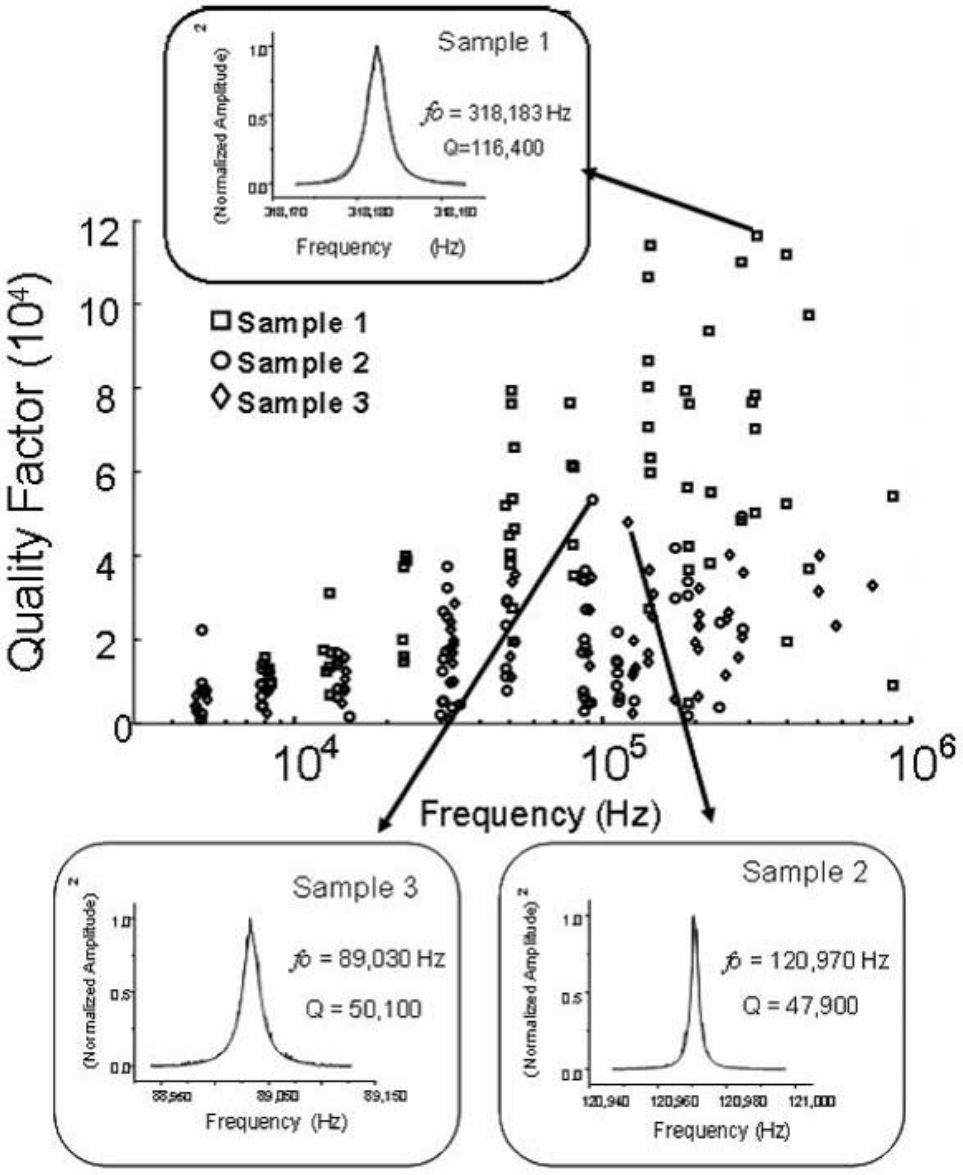

Fig. 5.9. Measured Q values as a function of frequency. Inset resonant peaks show the measurement with the highest Q value for each sample.

The measured Q values from samples 1-3 are plotted as a function of resonance frequency in Fig. 5.11 along with calculated Q values. The calculated Q values assume a Q limited by each of the three most common intrinsic and design-related energy dissipation mechanisms. The curves marked Q_{TED} and Q_{ph} are the expected maximum Q's if the energy dissipation was controlled by thermoelastic dissipation and phonon-phonon scattering, respectively [8]. The curve marked Q_{clamp} is the expected maximum Q if the energy dissipation was limited by clamping losses (mechanical damping by the beam support) [31]. The poly-C properties used for plotting the dissipation curves are shown in Table 5.3. All the Q values measured in this work are below any of the computed dissipation curves shown in Fig. 5.11, suggesting that the Q values are not limited by any of these dissipation mechanisms.

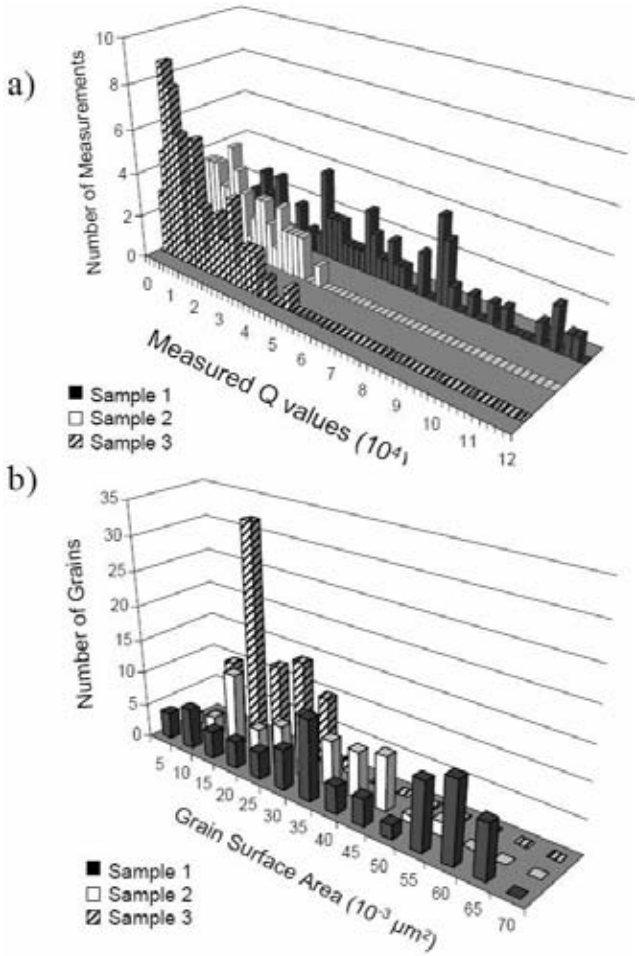

Fig. 5.10. a) Distribution of grain surface area for the 3 poly-C films. b) Distribution of measured Q values for the 3 poly-C films.

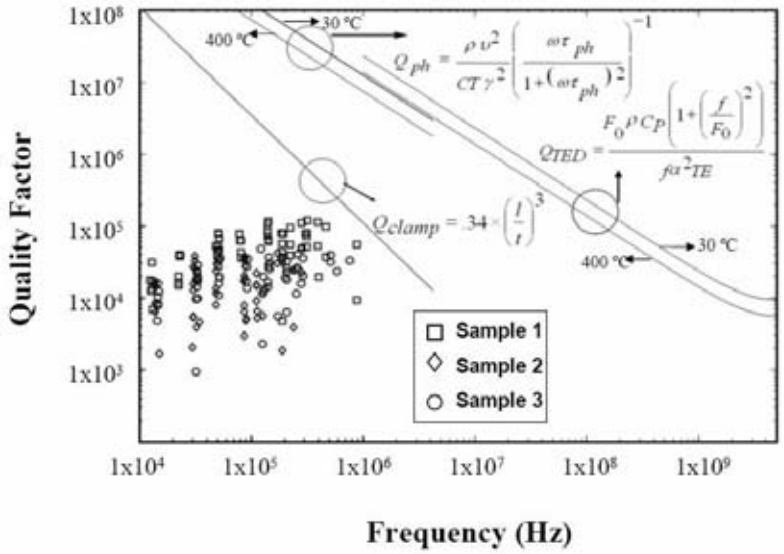

Fig. 5.11. Computed Q limiting curves and measured Q values for poly-C cantilever beams fabricated form the 3 studied samples. A thickness of 0.6 µm was used to plot the curves.

Table 5.3. Poly-C properties used to plot the Q limiting curves.

Parameter	Value
Thermal Expansion Coefficient, α (x 10^{-6} ºC^{-1})	1.1
Young's Modulus, E (GPa)	1,050
Density, ρ (kg m^{-3})	3520
Specific Heat Capacity, C_p (J kg^{-1}K^{-1})	502
Heat Capacity per Unit Volume, C (J m^{-3}K^{-1})	1.767
Thermal Conductivity, κ (W m^{-1} K^{-1})	1500
Gruneisen's Constant, γ	1
Velocity of longitudinal and transverse sound waves in the material υ_l ; υ_t	18 ; 13.1

In the absence of external defects (e.g. particles, processing film residue, etc.) the most likely mechanisms that limit Q values in polycrystalline materials are mechanical relaxation processes associated with defect motion, including vacancy motion, interstitial motion, dislocation motion, grain boundary sliding, etc. [7][8]. As the density of grains affects the amount of grain boundary defects that could be present in poly-C films, the distribution of grain sizes was investigated. If the dominant defects that cause internal dissipation were associated with grain boundaries, then we might expect that the films with the largest grain boundary area would show the lowest Q's. Fig. 5.10 shows the distribution of the grain cross-sectional area as measured at the sample surface for the three poly-C films, obtained using a procedure found in [32]. Samples 2 and 3 have, on the average, smaller grain sizes than sample 1. Although the grain sizes are larger for sample 1, the grain size distribution is large. As a result, it is difficult to estimate the absolute total grain boundary area of the three samples, but, qualitatively, the sample with the largest grains (sample 1) shows the highest Q's, suggesting that grain boundaries could play a role in limiting Q.

Most defect relaxation processes in polycrystalline materials have characteristic activation energies for defect motion [6]. If a single defect relaxation process dominates, it is often possible to determine the activation energy for defect motion by looking at the temperature dependence of Q. Most defects give a Debye-like relaxation, which limits the Q value according to the following equation [8]:

$$Q_{defect} = A\left[\frac{2\pi f\tau^*}{1+(2\pi f\tau^*)^2}\right]^{-1}, \qquad (5.3)$$

where f is the frequency and τ^* is the defect relaxation time. The defect relaxation time represents the average time needed for the defect to transition between two defect configurations. It is typically thermally activated with an Arrhenius relationship [8]:

$$\frac{1}{\tau^*} = \frac{1}{\tau_0} e^{\left(\frac{-E_A}{k_B T}\right)}, \qquad (5.4)$$

where $1/\tau_0$ is the characteristic atomic vibration frequency (about 10^{13} Hz), E_A is the activation energy for the relaxation process, T is temperature and k_B is the Boltzmann's constant. According to equation (5.3) Q will be minimum at the temperature at which $\tau^* = 1/2\pi f$, where, in this case, f represents the frequency of the resonator. Once τ^* is known, and assuming $\tau_0 = 10^{-13}$ sec, the activation energy for defect motion may be estimated using equation 5.4.

Fig 5.12 shows the measured Q values for samples 1-3 as a function of temperature. It can be noticed that the largest measured Q values for sample 2 show a minimum value at a temperature around 673 K, while the other two samples do not show a clear minimum for the highest measured Q values. This suggests that there is a dominant defect relaxation process in sample 2 which is peaked at a temperature of around 673 K. The absence of a minimum in Q for samples 1 and 3 suggests that there is likely a distribution of defect relaxation processes that are present, and no single defect process dominates. Assuming $\tau_0 = 10^{-13}$ sec, the minimum at 673 K for sample 2 would correspond to a defect activation energy of 1.7 eV. The most obvious source of possible defects that would be present in sample 2 and absent in samples 1 and 3 are defects associated with boron doping. Sample 2 is heavily doped (resistivity = 0.15 Ω-cm) whereas samples 1 and 3 are undoped. Whether the defect relaxation process is specifically associated with motion of the boron dopants or the motion of other defects that result from dopant incorporation in poly-C is not known. We do note that the activation energy for self-interstitial diffusion in crystalline diamond is 1.3 eV [33], and the activation energy for vacancy diffusion in crystalline diamond is 2.3 eV [34]. The value of 1.7 eV is in between these values but in a range where diffusional defect relaxation processes may be active.

The nanoresonators fabricated from poly-C exhibited frequencies and Q values in the range of 23 KHz – 53 KHz and 9,500 – 103,600, respectively. Fig. 5.13 shows SEM images of the thinnest fabricated poly-C nanocantilever along with the measured resonant peak. This nanocantilever had a length of 40 μm and a width of 100 nm. Since the width of this structure is smaller than the poly-C film thickness of 0.7 μm, the lowest frequency vibrational mode was parallel to the substrate. Therefore, the value for the beam width is used as the beam thickness in (5.1) to calculate the resonant frequency. Using a thickness of 100 nm, a length of 40 μm, a poly-C film Young's modulus of 990 GPa, a density of 3520 kg m^{-3} and using (5.1), the expected resonant frequency of this nanocantilever is 169,300 Hz. The resulting difference between the expected resonant frequency and the measured resonant frequency (183,214 Hz - 169,300 Hz = 13,914 Hz) could be due to errors in the beam dimensions, e.g. a trapezoidal beam cross-section as opposed to a rectangular cross-section. The ability to achieve and measure nanoresonators in poly-C films with surface topology exceeding 100 nm indicates that extremely small structures and devices can be successfully fabricated and utilized in polycrystalline diamond films.

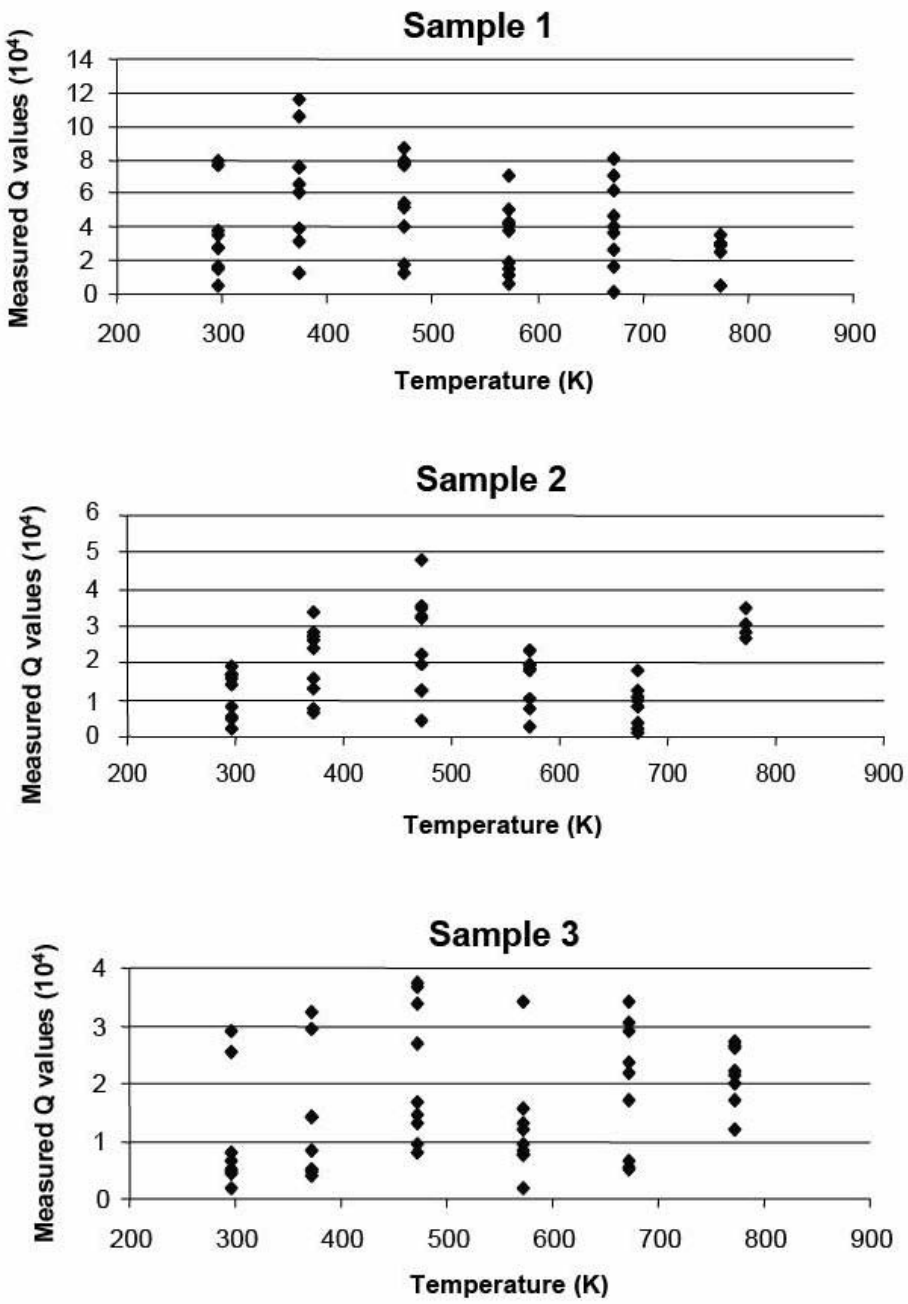

Fig. 5.12. *Measured Q values as a function of temperature for the three studied poly-C samples.*

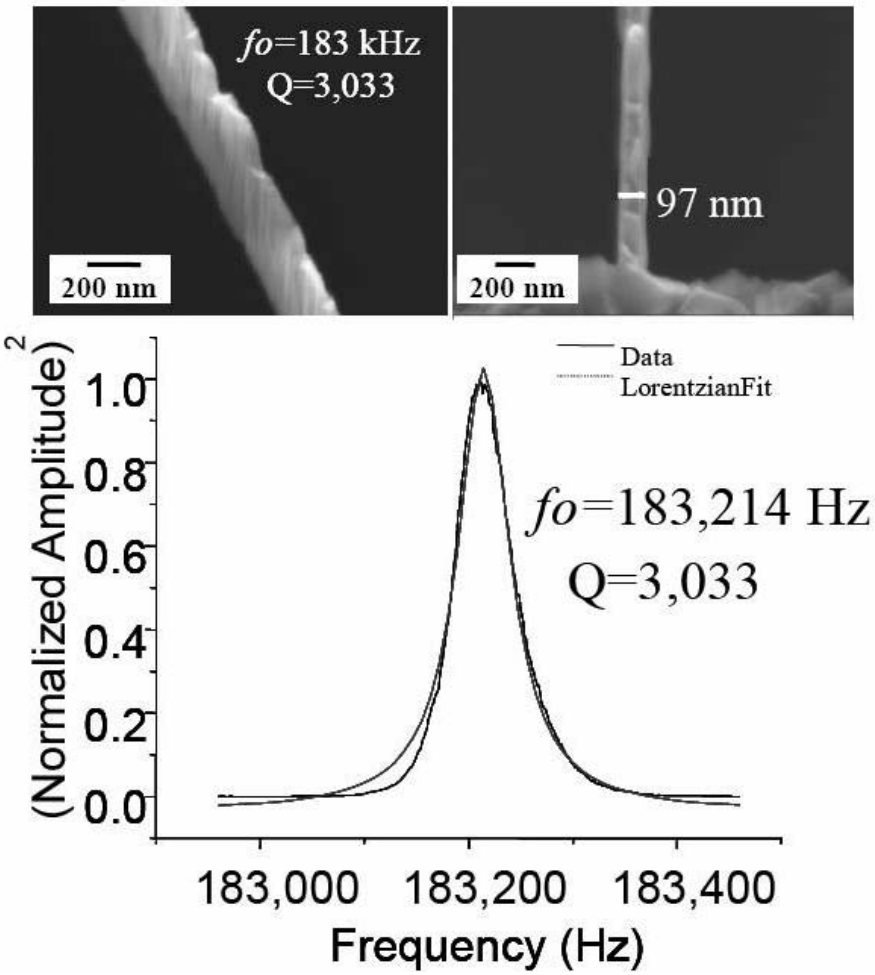

Fig. 5.13. SEM image and performance of a 100 nm wide polycrystalline diamond nano-cantilever.

5.5 Conclusions

In contrast to the amorphous carbon films discussed in the previous sections, polycrystalline diamond resonators exhibit much higher Qs. The highest Q values were observed for undoped poly-C films grown at 780 ºC. For boron doped poly-C films or poly-C films grown at a growth temperature of 600 ºC, lower Qs were observed. The doped poly-C film exhibited a peak in dissipation at 673 K, suggesting the existence of a dominant defect in these films that may be related to boron doping. The high Qs in all of the poly-C films suggest lower defect densities than found in amorphous films, which may be expected on the basis of the much higher degree of order in crystalline materials. This suggests that the amorphous network of amorphous carbon is able to support a large number of defect relaxation processes that may involve individual or large collections of atoms.

The temperature dependence of the poly-C resonators was also examined, and a temperature coefficient of resonance frequency in the range of -1.59×10^{-5} to -2.56×10^{-5} °C^{-1} was observed. We also report the smallest patterned poly-C nanoresonator structure, a cantilever resonator that is 100 nm wide, 0.7 μm thick and 40 μm long.

Nelson Sepulveda received financial support for this work during his time at Michigan State University through the Bill and Melinda Gates foundation

5.6 References

[1] S. S. Li, Y. W. Lin, Y. Xie, Z. Ren, and C. T-C. Nguyen, IEEE Int. Conference on MEMS pp.821-824, 2004.

[2] K. Wang, A. C. Wong, C. T.-C. Nguyen, J. MEMS **9**, 347 (2000).

[3] W.T. Hsu and C. T.-C. Nguyen "Geometric stress compensation enhanced thermal stability in micromechanical resonators" IEEE Transactions ultrasonics simposium, Sendai, Japan, pp. 945-948, Oct. 5-8, 1998

[4] W.T. Hsu, S. Lee, and C. T.-C. Nguyen "*In Situ* annealing for contamination resistance and enhanced stability in Nickel Micromechanical resonators" International Conference on Solid-State Sensors and Actuators, pp.932-935 June 7-10 1999.

[5] S. Evoy, D. W. Carr, L. Sekaric, A. Olkhovets, J. M. Parpia, and H. G. Craighead, "Nanofabrication and electrostatic operation of single-crystal silicon paddle oscillators" *Journal of Applied Physics*, vol.86, pp. 6072-6077, 1999.\

[6] A.S. Nowick and B.S. Berry "Anelastic relaxation in crystalline solids", New York, Academic Press, 1972.

[7] D. Czaplewski, J.P. Sullivan, T.A. Friedmann, D.W. Carr, B.E.N. Keeler and J.R. Wendt; *Journal of Applied Physics*, vol.97, 023517, 2005.

[8] V. B. Braginsky, V. P. Mitrofanov, V. I. Panov, K. S. Thorne, *Systems with Small Dissipation,* The University of Chicago Press, 1985.

[9] X. Zhu, D. M. Aslam, Y. Tang, Stark B.H., K. Najafi, "The fabrication of all-diamond packaging panels with built-in interconnects for wireless integrated microsystems" *Journal of Microelectromechanical Systems* vol. 13, pp. 396-405, June 2004.

[10] X. Zhu, D.M. Aslam, "Polycrystalline diamond thin film packaging technology for wireless integrated microsystems" IEEE Solid-State Sensors, Actuators and Microsystems, vol 1, pp.912-915, June 2005.

[12] N. Sepulveda-Alancastro and D. M. Aslam, "Polycrystalline diamond technology for RFMEMS resonators," *Microelectronic Engineering*, vol. 73-74, pp. 435-440, 2004.

[13] N. Sepulveda, D.M. Aslam, J.P. Sullivan, "Polycrystalline Diamond MEMS Resonator Technology for Sensor Applications" *Diamond and Related Materials*, Currently in press.

[14] J. Wang, J. E. Butler, D. S. Y. Hsu and C. T.-C. Nguyen "CVD Polycrystalline diamond high-Q micromechanical resonators" IEEE International Conference Micro Electro Mechanical Systems. pp. 657-660, 2002

[15] J. Wang, J. E. Butler, D.S.Y. Hsu, and C. T. –C. Nguyen, "High-Q Micromechanical resonators in CH4-reactant optimized high acoustic velocity polydiamond" Tech. Digest, 2002 Solid-State Sensor, Actuator and Microsystems Workshop, Hilton Head Island, South Carolina, pp. 61-62, June 2-6, 2002,

[16] W. T. Hsu; C.T.-C. Nguyen, "Stiffness-compensated temperature-insensitive micromechanical resonators" IEEE Int. Conference on MEMS, pp.731 – 734, Jan 20-24 2002.

[17] W. T. Hsu; J.R Clark,.; C.T.-C Nguyen,.; "Mechanically temperature-compensated flexural-mode micromechanical resonators" Electron Devices Meeting, International pp. 399 – 402, Dec 10-13 2000

[18] L. Sekaric, J.M. Parpia, H.G. Craighead, T. Feygelson, B. H. Houston and J. E. Butler. "Nanomechanical resonant structures in nanocrystalline diamond"; *Applied Physics Letters*, Vol. 81, pp.4455-4457, December 2002.

[19] A. B. Hutchinson, P. A. Truitt and K. C. Schwab, L. Sekaric, J. M. Parpia, H. G. Craighead and J. E. Butler; "Dissipation in nanocrystalline-diamond nanomechanical resonators" *Appl. Phys. Lett* 84 (6) pp.972-974, 2004

[20] S. Roy, R.G. DeAnna, C.A. Zorman and M. Mehregany "Fabrication and Characterization of Polycrystalline SiC Resonators" *IEEE Transactions on Electron Devices*, vol. 49, No.12 December 2002.

[21] J. Wang, J. E. Butler, Tatyana Feygelsonand C. T.-C. Nguyen "1.51-GHz Nanocrystalline diamond micromechanical disk resonator with material-mismatched isolating support" IEEE Int. Conference on MEMS pp.731 – 734, 2004.

[22] Y. Tang and Dean M. Aslam "Technology of polycrystalline diamond thin films for microsystems applications" *Journal of Vacuum Science and Technology* B23(3) pp. 1088-1095, May/Jun 2005

[23] A. Masood, "Polycrystalline diamond films for temperature sensing", Ph.D. Dissertation, Michigan State University, 1992.

[24] J. Yang, T. Ono, and M. Esashi, "Mechanical behavior of ultrathin micro-cantilever," *Sens. Actuators*, vol. 82, pp. 102–107, 2000.

[25] J. Yang, T. Ono, and M. Esashi, "Energy Dissipation in Submicrometer Thick Single-Crystal Silicon Cantilevers" *Journal of Microelectromechanical Systems* Vol. 11, pp.775-783 Mar. 2000.

[26] P. J. Petersan and S. M. Anlage, "Measurement of resonant frequency and quality factor of microwave resonators: Comparison of methods" *Journal of Applied Physics*, vol. 84, pp. 3392-3402, 1998

[27] W. Weaver, S. P. Timoshenko, and D. H. Young, *Vibration Problems in Engineering*, 5th ed: Wiley Publishers, 1990

[28] H. J. McSkimin and P. Andreatch Jr, "Elastic Moduli of Diamond as a Function of Pressure and Temperature" *Journal of Applied Physics*, vol. 43, pp. 2944-2948, July 1972.

[29] W. N. Sharpe, Jr., M.A. Eby, and G. Coles, "Effect of Temperature on Mechanical Properties of Polysilicon", Proceedings Transducers '01, Munich pp. 1366-1369 2001.

[30] F. Szuecs, M. Werner, R. S. Sussmann, C. S. J. Pickles, and H. J. Fecht "Temperature dependence of Young's modulus and degradation of chemical vapor deposited diamond" *Journal of Applied Physics*, vol. 86 no 11 pp. 6010-017, December 1999.

[31] H. Hosaka, K. Itao, and S. Kuroda, Sens. Actuators A **49**, 87 (1995).

[32] S. Sahli and D. M. Aslam, "Nonuniform conduction in B-doped chemical vapor deposited diamond studied by intra- and intergrain measurements" *Appl. Phys. Lett* 70 (16) pp.2129-2131, 2004

[33] J. F. Prins, "Point-defect interactions when annealing diamonds implanted at low temperatures" *Physical Review B*, vol. 44, pp. 2470-2479, 1991.

[34] G. Davies, S. C. Lawson, A. T. Collins, A. Mainwood, S. J. Sharp, "Vacancy-related centers in diamond" *Physical Review B* **46**, 13157-13170 1992.

6.0 Modeling of Defect-Related Internal Dissipation

6.1 Summary

Numerical modeling of defect-related internal dissipation processes in silicon-based nanoresonators was performed in order to elucidate the atomic scale mechanisms associated with the dissipation of mechanical energy. Three types of nanoresonator structures were studied. One system consisted of a resonator of crystalline silicon, another system consisted of a resonator of amorphous silicon, and the third system was a crystalline silicon resonator containing a single atomic-scale defect. The simulations showed that the amorphous system and system with a single defect exhibited much higher dissipation than the pure crystalline silicon system, indicating that the internal dissipation was defect-controlled, as is consistent with the experimental observations in the prior sections. In addition, temperature-dependent dissipation studies were performed on the crystalline silicon and crystalline silicon system with single defect. The preliminary findings indicated the defect system exhibited consistently higher dissipation at all temperatures, but a Debye-like loss peak was not observed over the temperature range of study (300 K to 700 K).

6.2 Background

There is a significant amount of experimental evidence that internal dissipation in micron to sub-micron resonators is controlled by defect relaxation processes.[1-4] The difficulty with these experimental systems is that the nature of the defect relaxation processes are poorly understood. At best, the experiments suggest activation energies for relaxation processes, which could correspond to single atom hopping, bond reorientation, collective atom motion, or diffusional processes.[5] The advantage of numerical simulation is that it affords a possibility of studying the defect relaxation process at the atomic scale with a well-defined system. There has been relatively little work in the theoretical study of mechanical dissipation processes. Jiang et al. reported a numerical study of internal dissipation in an ideal (defect-free) single wall carbon nanotube rigidly supported on one end.[6] Their work showed a surprising excess dissipation down to very low temperature, despite the absence of defects in the nanotube. This effect remains unexplained and suggests the need for careful studies of the mechanism of the relaxation process, which is a goal of this study.

6.3 Simulation Procedure andResults

Theoretical simulations were performed on systems of several hundred up to a few thousand silicon atoms possessing either amorphous or crystalline structure with and without an isolated defect. For the amorphous structure, high quality (low density of coordination defects) amorphous silicon unit cells were obtained via collaboration with N. Bernstein (NRL). Unit cells for atomistic simulation were obtained by tiling 216 atom unit cells in a chain to create 216, 432, and 864 atom cells (see Figure 6.1 for one of these cells: the physical size of this 432 atom unit cell is approximately $16.5 \times 16.5 \times 33$ Å). The crystalline cell and crystalline cell plus defect contained 2000 and 2001 atoms, respectively, in a rectangular cell of dimensions $27.4 \times 27.4 \times 54.8$ Å. The defect in silicon was chosen to be a split interstitial defect. This defect was chosen because it has lower symmetry than the Si lattice, and, hence, it can couple to the strain field

created by the mechanical vibration. Furthermore, based on *ab initio* calculations using Density Functional Theory (DFT), this defect relaxes by moving one Si atom into a 6-fold interstitial site, and the approximate activation energy for defect hopping is 0.16 eV. Therefore, this defect would be expected to undergo multiple relaxation steps (hops) per nsec at a simulation temperature greater than 400 K. An estimate of the defect relaxation time, τ^*, is given by Equation 6.1:

$$\frac{1}{\tau^*} = \frac{1}{\tau_0} e^{\left(\frac{-E_A}{k_B T}\right)} , \qquad (6.1)$$

where $1/\tau_0$ is the characteristic atomic vibration frequency (about 10^{13} Hz), E_A is the activation energy for the relaxation process, T is temperature and k_B is the Boltzmann's constant. Using E_A = 0.16 eV, and T = 400 K, we obtain τ^* = 10 psec. Figure 6.2 shows the atomic structure of the split interstitial defect and the unit cell containing the defect used for simulation.

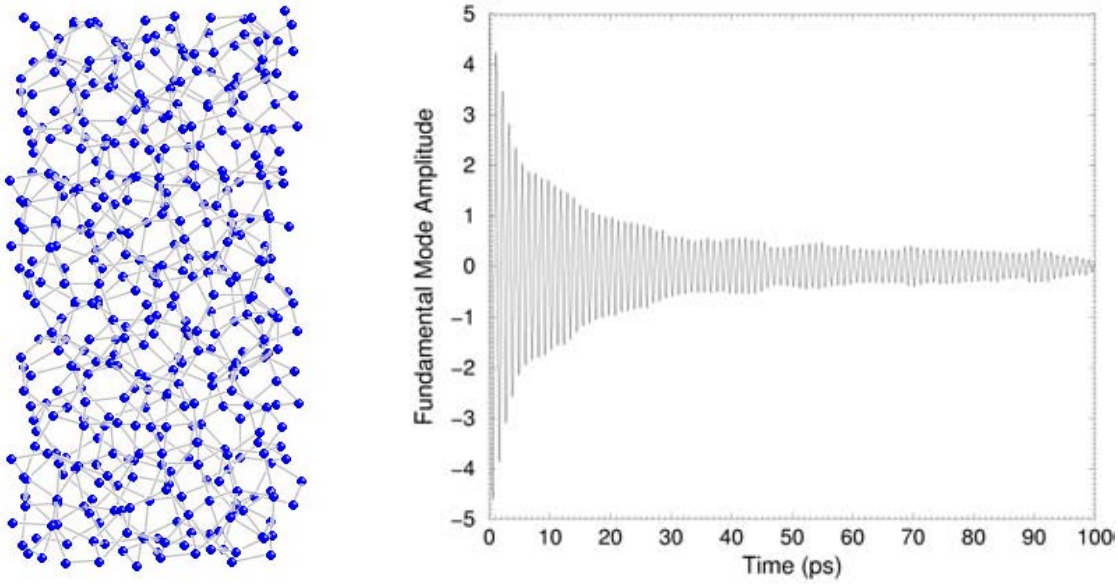

Fig. 6.1. A 432 atom amorphous silicon unit cell and the ring-down plot from which Q is determined for the lowest resonance mode in this system. Q was found to be 3.6, more than two orders of magnitude lower than crystalline silicon using the same simulation conditions.

Ring-down simulations were performed to quantify internal dissipation in the nanoresonator systems. These simulations involved exciting one particular mechanical vibration and observing the decay in amplitude of this vibration over time. In a classical ring down experiment, the amplitude decays exponentially with time, and Q is determined from

$$E(t) = E_0 e^{\left(\frac{-\omega t}{2\pi Q}\right)} , \qquad (6.2)$$

where E(t) is the energy in the vibration mode at time t, E_0 is the initial energy, and ω is the angular frequency of the mode. The result of one of these ring-down measurements is shown in Figure 6.1. For the 432 atom cell of Figure 6.1, the quality factor was found to be 3.6 ± 0.2 at 943 GHz.

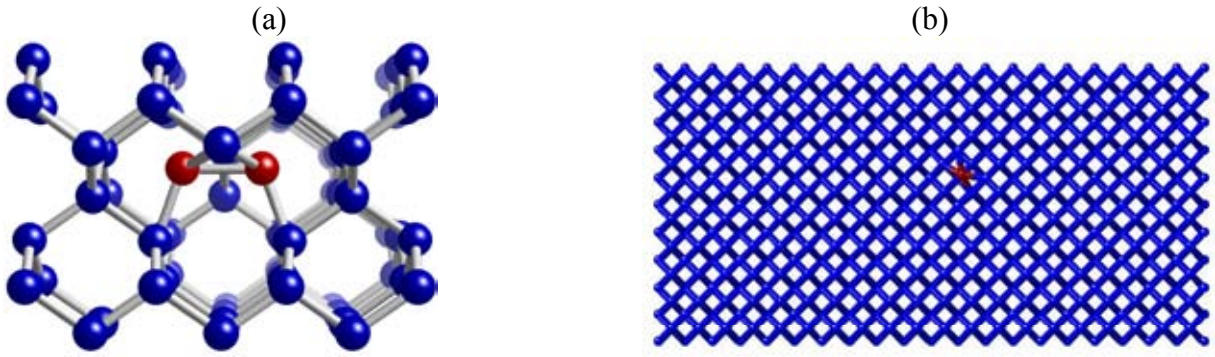

Fig. 6.2. a) Atomic structure of the split interstitial defect in silicon (Si interstitials are in red), and b) the unit cell with defect (in red) used for the internal dissipation simulation.

The dynamics of the systems were evaluated using molecular dynamics (MD) employing classical potentials. For this work, we used the Environment Dependent Interatomic Potentials (EDIP).[7-9] Periodic boundary conditions were used on each boundary of the cells. The systems were equilibrated using constant temperature MD. This was repeated at each simulation temperature used (from 300 K up to 700 K in increments of 100 K). Following equilibration for each system and each temperature, the Lanczos method was used to find the lowest eigenvectors and eigenvalues of the dynamic matrix.[10] In the crystalline Si system this yields four degenerate lowest vibrational modes corresponding to the 2 transverse acoustic modes with even and odd (cosine and sine) matching at the boundaries. The longitudinal acoustic mode lies higher in energy. Following identification of the lowest vibrational modes, the energy of one mode was increased by a scalar multiplication of the velocity of the atoms associated with the eingenvector of that mode. The energy input into this mode was approximately 100 times higher than the thermal energy in the system. Then constant energy MD was used on the excited system for 8×10^6 time steps, representing a total elapsed time of greater than 2100 psec. During this MD simulation, snap shots were taken after every 50 time steps, and the velocities were projected onto the 4 identified lowest modes. Due to degeneracy between these modes, there was significant transfer of energy between modes, necessitating an accounting of each mode. For each mode at each snap shot, an average energy of the mode was computed, and these mode energies as a function of time are shown as colored lines in Figure 6.3. These individual mode energies were then summed to give the total energy in the vibrational mode, which is shown in black in Figure 6.3. An exponential fit to the total energy, shown as the red curve in Figure 6.3, was performed in order to obtain Q for the resonator.

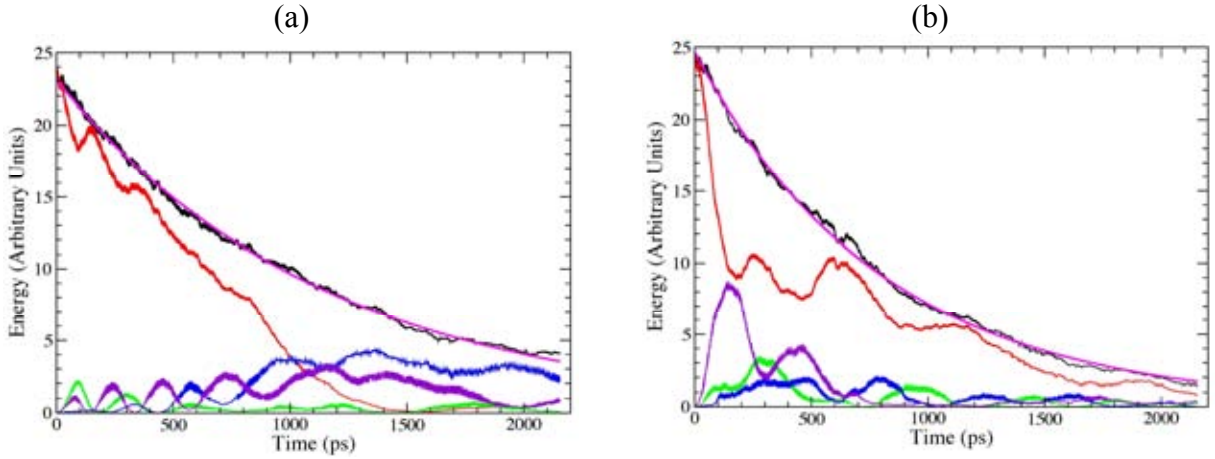

Fig. 6.3. Ring down plots at 300 K for crystalline silicon without defects (a) and with a split interstitial defect (b). The colored curves show the total energies in the four nearly degenerate vibrational modes. The black line is the sum of the total energies, and the red curve is an exponential fit. The Qs were found to be 1120 and 790 for the defect free and single defect systems, respectively.)

In order to determine the temperature dependence of internal dissipation, the ring down simulations were performed at discrete temperatures up to 700 K. At each temperature, the total energy in the vibrational mode was determined, and exponential fits were used to determine Q (see Figure 6.4). From these plots, the Q vs temperature was obtained for crystalline silicon with and without a defect (see Figure 6.5).

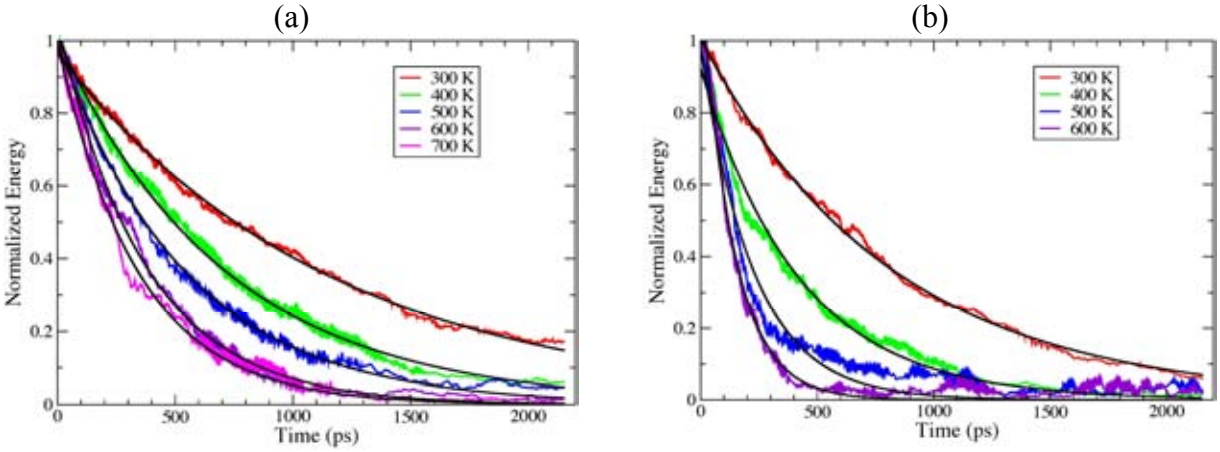

Fig. 6.4. Ring down plots at various temperatures for crystalline silicon without defects (a) and with a split interstitial defect (b). The colored curves show the total energies in the vibrational modes, and the black lines are exponential fits.

The ring down simulations clearly show the enhanced dissipation due to defect relaxation processes. This is especially pronounced for amorphous silicon, where the Q was over two orders of magnitude lower than the Q of the crystalline silicon system (Fig. 6.1). For the amorphous cell, tests were performed on scaling of Q with cell size. An amorphous cell twice as large as that shown in Fig. 6.1 (a total of 864 atoms and a cell length 66 Å long) showed a Q

approximately twice as large (at a resonant frequency about half as high). This scaling is consistent with the extremely short phonon mean free paths that are expected in amorphous systems. Unfortunately, the complicated dynamics of the amorphous cell do not permit easy identification of discrete defect relaxation events. For this reason, effort was put into indentifying defect relaxation dynamics in simpler systems.

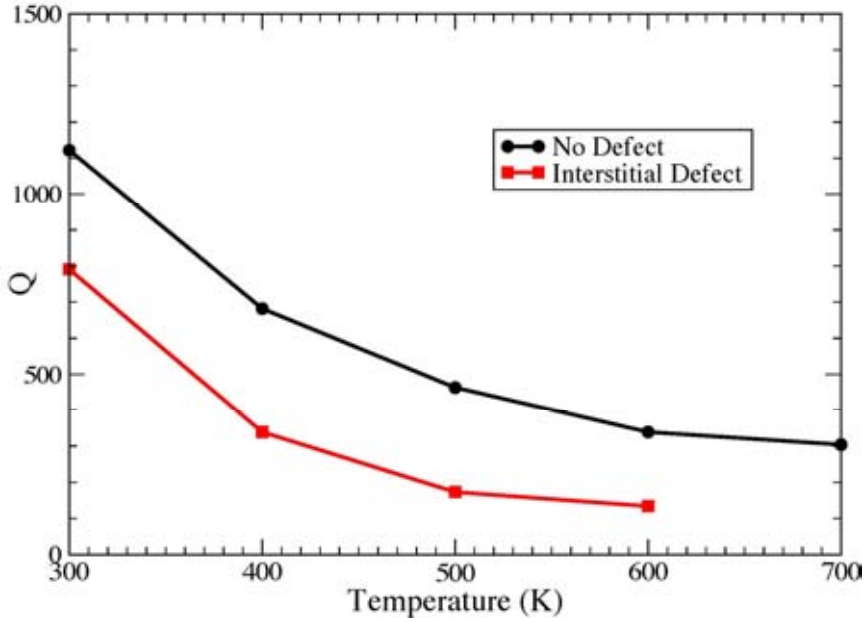

Fig. 6.5. Q versus temperature as determined by ring down simulations for silicon without defects (black curve on top) and silicon with a split interstitial defect (red curve).

The silicon split interstitial defect is an ideal defect for study due to its low symmetry and modest activation energy for defect hopping (~ 0.2 eV). MD simulations revealed that defect hopping was appreciable at 400 K with increased hopping expected at 500 K. A maximum in internal dissipation (a minima in Q) is expected when the defect relaxation rate, 1/t*, equals the vibrational frequency of the resonator. For the silicon unit cells with and without a split interstitial defect, the vibrational frequencies ranged from 980 GHz at 300 K to 940 GHz at 600 K and from 980 GHz at 300 K to 933 GHz at 700 K, respectively. At these frequencies, a peak in dissipation would be expected at about 800 to 900 K for an assumed defect activation energy of 0.16 eV (see Eq. 6.1). While the internal dissipation was higher for the system with a defect at all temperatures studied, we did not observe a clear maximum in dissipation which would signal the presence of a Debye-like loss peak in the temperature range up to 600 K. Additional simulations at higher temperatures will be necessary to determine if a defect resonance occurs. Nevertheless, the single defect is found to limit the Q in the system, reducing the Q by as much as 60% at a temperature of 600 K. Table 6.1 summarizes the observed Qs for the defect-free and isolated defect systems.

Table 6.1. Q as a function of temperature for a crystalline silicon system that is defect free and a crystalline silicon system containing a single split interstitial defect. The error in Q can be as high as ±50.

Simulation temp.	Q without defect	Q with defect
300 K	1120	790
400 K	680	340
500 K	460	170
600 K	340	130
700 K	300	

6.4 Conclusions

Numerical simulation of internal dissipation in amorphous silicon, defect-free crystalline silicon, and defect-containing crystalline silicon nanoresonators revealed strong enhancement of dissipation in the presence of defects. Amorphous systems showed quality factors more than two orders of magnitude lower than the crystalline system at frequencies approaching 1 THz. Experimentally, the quality factor of amorphous carbon was found to be up to 1.5 orders of magnitude lower than the quality factor of high quality polycrystalline diamond.[2][4] Numerous defect relaxation processes may be present in amorphous systems, which inhibits the ability to isolate specific defect relaxation mechanisms. A model study involving a single split interstitial defect in crystalline silicon revealed that there is a strong reduction in quality factor up to 60% with the existence of a single defect. A temperature-dependent study of internal dissipation in this system showed that the internal dissipation is higher over the entire temperature range that was studied (300 K to 700 K) for the system with defect, but no strong defect resonance was observed. One possibility is that the defect resonance would occur at a higher temperature than the range of study.

6.5 References

[1] D.A. Czaplewski, J.P. Sullivan, T.A. Friedmann, D.W. Carr, B.E.N. Keeler, and J.R. Wendt, J. Appl. Phys. **97**, 023517 (2005).

[2] D. A. Czaplewski, J. P. Sullivan, T. A. Friedmann, J. R. Wendt, Diamond and Rel. Mater. **15**, 309 (2006).

[3] N. Sepulveda, D. Aslam, and J. P. Sullivan, Diamond and Rel. Mater. **15**, 398 (2006).

[4] N. Sepulveda, D. M. Aslam, and J. P. Sullivan, submitted to J. MEMS (2006).

[5] A. S. Nowick and B. S. Berry, *Anelastic Relaxation in Crystalline Solids* (Academic Press, Inc., New York, 1972).

[6] J. Jiang, M.-F. Yu, B. Liu, and Y. Huang, Phys. Rev. Lett. **93**, 185501 (2004).

[7] M. Z. Bazant and E. Kaxiras, Phys. Rev. Lett. **77**, 4370 (1996).

[8] M. Z. Bazant, E. Kaxiras, J. F. Justo, Phys. Rev. B **56**, 8542 (1997).

[9] J. F. Justo, M. Z. Bazant, E. Kaxiras, V. V. Bulatov, and S. Yip, Phys. Rev. B **58**, 2539 (1998).

[10] J. K. Cullum and R. A. Willoughby, *Lanczos algorithms for large symmetric eigenvalue computations* (Birkhäuser, Boston, 1985).

7.0 Coupled Mechanical Oscillators

7.1 Summary

Both one-dimensional (1D) and two-dimensional (2D) coupled oscillator arrays have been fabricated in amorphous and polycrystalline diamond materials. The 1D arrays consisted of a row of cantilever oscillators having nominally identical dimensions and their lowest vibrational mode in the plane of the film. This geometry should exhibit weak mechanical coupling between the elements. The 2D coupled oscillator arrays were fabricated out of tetrahedral amorphous carbon with elements arranged on a square lattice. The lowest vibrational modes were drumhead modes owing to the regularity of the array (absence of defects). Numerical simulations showed that the 2D arrays should exhibit localized vibrational states centered at regions of disorder in the array. Designs for disordered coupled oscillator arrays have been developed to experimentally test these ideas.

7.2 Introduction and Background

In other sections of this report, we have focused on internal dissipation in mechanical systems, and coupled oscillator arrays offer unique insight into some dissipation mechanisms. In addition to defect-related internal dissipation mechanisms that have been discussed in prior sections of this report, coupled arrays exhibit dissipation due to mechanical coupling between neighboring oscillator elements. Mechanical energy in one oscillator may be transferred to a neighboring oscillator in the form of mechanical energy, analogous to the energy transfer between degenerate vibrational states that was observed in the numerical simulations of Section 6. The transfer of energy between mechanical elements may be regular or chaotic, rendering the dynamics of any individual oscillator difficult to predict. Therefore, it is important to follow the dynamics of the entire coupled oscillator array, which necessitates experimental approaches that permit mapping of vibrational states over a spatial region (i.e. 2D mapping). Some preliminary work in this area will be discussed in this section.

In addition to the interesting dissipation dynamics of coupled systems, it is useful to consider the non-dissipative behavior of coupled mechanical systems. For example, a large coupled oscillator array is essentially a classical analog of a two-dimensional atomic crystal. Hence, conventional thermodynamic and statistical mechanical descriptions may be applied. For example, the spectrum of eigenmodes of the array is the phonon spectrum of a 2D lattice. A sufficiently large mechanical impulse that excites a large number of eigenmodes of the array is analogous to the application of a heat pulse to the 2D crystal. Due to coupling between the eigenmodes of the array (from anharmonic effects), it is expected that the initial spectrum of eigenmodes should relax to a thermalized spectrum with the population of eigenmodes following Bose-Einstein statistics with a temperature, T' – the effective temperature of the array of coupled oscillators. The relaxation time for this process is analogous to the relaxation time for phonons to reach thermal equilibrium in a 2D lattice. The mechanical energy (heat) stored in the coupled oscillator array is transferred, due to internal dissipation in the springs, into the heat bath (the material that makes up the springs and the islands) leading to an increase in the real temperature, T, of the coupled oscillator array.

The “effective heat capacity” of the array can be thought of as the amount of mechanical energy that is required to be added to increase the effective temperature of the array by an

amount $\Delta T'$ (as measured by the population of eigenmodes). The thermal expansivity of the coupled oscillator array – a measure of the anharmonicity of the springs – can be thought of as the increase in mean squared separation between elements of the array with increasing T', and should be measurable by light diffraction. Whether any of these effects are observable depends on the relative coupling between eigenmodes of the array and the coupling of the array itself with its heat bath. If internal dissipation is high, then most of the mechanical energy of the array would be dissipated as heat before "thermalization" of the eigenmode spectrum could occur.

The assumption for this discussion concerning coupled oscillator arrays has been that the elements of the array are identical and, hence, the collective properties of the array, eigenmode spectrum, etc., would be that of an ideal, perfect lattice. In reality, a variety of "lattice defects" might be expected to be present in the real coupled oscillator system. These defects include irregularity in the location of elements of the array, heterogeneity in the masses of the springs and islands of the array, heterogeneity in the spring constants (e.g. due to variations in the dimensions of the springs), and heterogeneity in the internal dissipation of the springs. These defects can all be grouped together as various forms of disorder of the coupled oscillator lattice. One of the dominant effects of disorder is that the eigenstates of the system, whether electronic, photonic, or acoustic may become localized. Localization in disordered periodic lattices, first considered in electronic systems by Anderson, has become known as Anderson localizaton [1]. Shortly after Anderson's work, theories of localization were applied to phonon localization in random lattices [2] and, later, to localization of acoustic waves in macroscopic systems of disordered scatterers [3]. Of direct interest to our study of 2D coupled oscillator arrays, Williams and Maris have performed numerical studies of phonon localization for 2D square lattices with mass disorder [4], and He and Maynard have considered localization experimentally in a 1D system consisting of an array of masses attached to a vertically suspended steel wire [5]. In order to see localization due to mass disorder in the simulated 2D lattice, Williams and Maris found it necessary to consider significant variation in mass, $> \pm 25\%$ deviation from the average mass [4]; similarly, He and Maynard found that small variations in the masses ($\sim \pm 13\%$) in their experimental 1D system (which is more sensitive to localization) did not lead to localization in the transverse waves of the vibrating wire [5]. In contrast, small variations in the position of the masses in He and Maynard's experiment (changes in mass-to-mass distance) of $\pm 2\%$ did lead to strong localization of the transverse waves [5]. With this insight, we might predict that localization of the vibrational modes of the 2D coupled oscillator array would be most sensitive to site (positional) disorder of the array elements.

Site or positional disorder is not expected to be the dominant defect in as-fabricated 2D oscillator arrays, however, as the spacing between elements can be well-controlled during the lithography steps [6]. The degree of positional disorder can be verified through measurements of the width of Bragg peaks from light diffraction off of the arrays. There is expected to be variation in the masses of the elements and the dimensions of the springs, however, due to the standard variations in resist-based lithography and etching processes as well as to unintended defects, such as particulates, in the array. Provided these variations can be kept small ($<\pm 10\%$), this heterogeneity is not expected to be a major contributor to localization. An alternative form of disorder could arise from variations in internal dissipation of the nano-scale springs themselves (Q disorder). The sensitivity of localization to Q disorder is not presently well-understood. However, since the internal dissipation is a materials property, it is not expected to vary substantially between elements (at least for higher temperatures and larger sample sizes where, statistically, the number of defects per oscillator is similar).

Static disorder is not required for localization in the array. When driven to sufficiently high amplitudes, a non-linear mechanical response of the spring elements can be achieved. Coupling to an external driver can result in the stabilization of local vibrational modes. In this case, the position of the localized mode is strongly dependent on the initial mechanical noise in the system. This type of localization has recently been observed in 1D arrays of bi-element cantilever oscillators [8].

Coupling of non-linear oscillators to mechanical noise (stochastic resonance) is a major research topic in fields such as biology (e.g. useful for understanding the dynamics of neural networks). Non-linear elements can be incorporated in the oscillator arrays through the inclusion of bistable oscillators. There is considerable expertise in bistable mechanical elements fabricated in MEMS systems at Sandia, leading to the possibility of fabricating arrays of bi-stable oscillator elements. Studies of the dynamics of these systems may lead to improved understanding of neural networks or of coupled sensor arrays (sensor systems in which the collective output depends on communication between individual sensors).

7.3 Experiment and Results

A variety of 1D oscillator arrays were fabricated in amorphous and polycrystalline diamond, see Fig. 7.1 for an example of 1D oscillator array fabricated from polycrystalline diamond. The 1D arrays consisted of singly-clamped beams (cantilever oscillators) that were fabricated using the micro- and nano-fabrication procedures described in the prior sections. These oscillators have their lowest frequency vibrational mode (simple flexure) that is confined in the plane of the film. This geometry is different than the oscillator array of Sato, et al., wherein the dominant vibrational mode is perpendicular to the plane of the film [8]. These types of arrays are expected to have greater mechanical coupling between elements due to the low stiffness (high compliance) at the oscillator supports. A large degree of mechanical coupling was indeed observed by Sato et al.[8] Our measurements of the in-plane 1D oscillator arrays were limited in their ability to detect the vibrational dynamics of the entire array due to our use of laser interferometry that provides only single point detection of vibrational amplitude. Therefore, the rest of this section is focused on the 2D coupled oscillator designs.

Two different designs for 2D coupled oscillator designs were designed and fabricated in this work. The first design consisted of a 10×10 array of oscillator elements, wherein the oscillator is defined as a node in a grid fabricated from tetrahedral amorphous carbon (ta-C) having a tungsten proof mass on top, see Fig. 7.2. The grid lines were patterned to be 500 nm wide using e-beam lithography, while the tungsten ($\sim 1\ \mu m \times 1\ \mu m$) was defined using a separate e-beam lithography step. The patterning of the tungsten proof mass required an alignment step, resulting in occasional alignment error (as is shown in the inset of Fig. 7.2). In the second design, we expanded the number of elements by a factor of 100, creating 100×100 element arrays. Fabrication of these arrays was very successful with better alignment of the tungsten proof mass over the grid nodes, see Fig. 7.3.

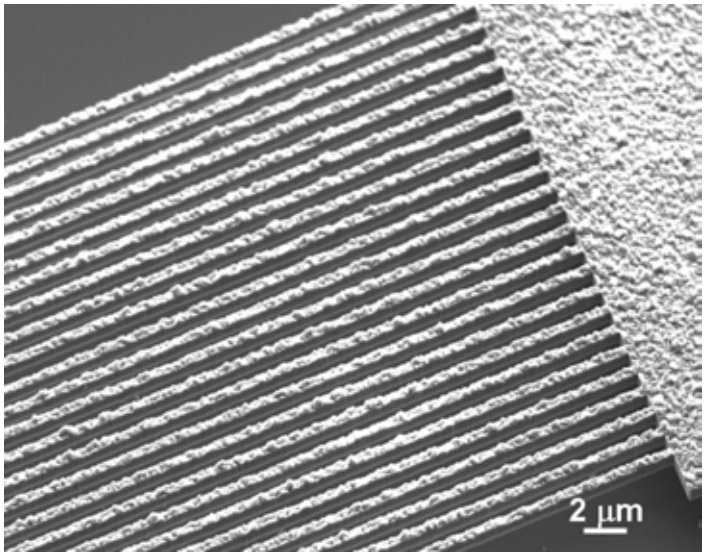

Fig. 7.1. 1D array of 25 polycrystalline diamond cantilever oscillators with a dominant in-plane resonance mode.

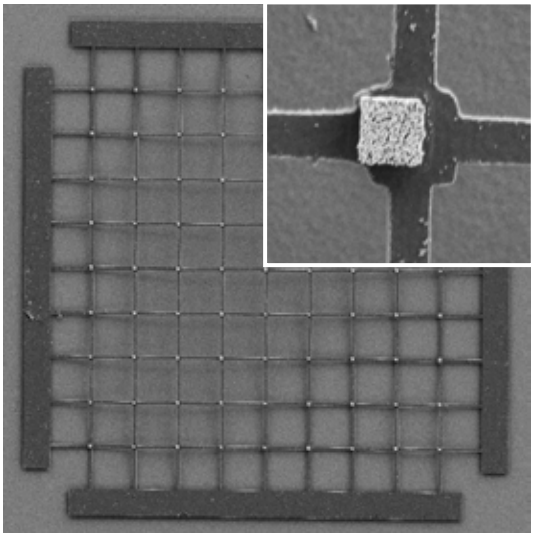

Fig. 7.2. A 10 × 10 coupled oscillator array fabricated from ta-C and W. The inset shows the alignment of one of the W islands (bright square) with the node in the grid of the array.

These oscillator arrays exhibit vibrational modes similar to drumhead modes of a stretched membrane. A modal analysis of the 10 × 10 array was performed using the ANSYS mechanical modeling package, and several of the lowest frequency vibrational modes are shown in Fig. 7.4. Resonance testing of the arrays revealed a series of resonance peaks, where the lowest frequency peaks were in reasonable agreement with the modal analysis using ANSYS. The use of laser interferometry at a single point precluded accurate identification of the modes in most cases, particularly as the vibrational amplitude is a strong function of position on the array (see Fig. 7.4). Through a collaboration with Polytec corporation, scanning laser Doppler vibrometry (LDV) was able to confirm the approximate mode frequencies. A still frame from a digital movie of the second lowest vibrational mode of the 10 × 10 array is shown in Fig. 7.5. This mode has a diagonal nodal line – one diagonal quadrant of the array undergoes deflection

upwards out of the plane while the opposite quadrant is deflected below the plane (which is clear when represented as a movie). The measured resonant frequency of 486 KHz is close to the expected resonance frequency based on the simulation (Fig. 7.4). Measurements made on the 100 × 100 array revealed a number of resonance modes, but the identification of the modes was not possible using single point detection. Scanning laser Doppler vibrometry would be needed to permit mode identification, and these experiments are being pursued.

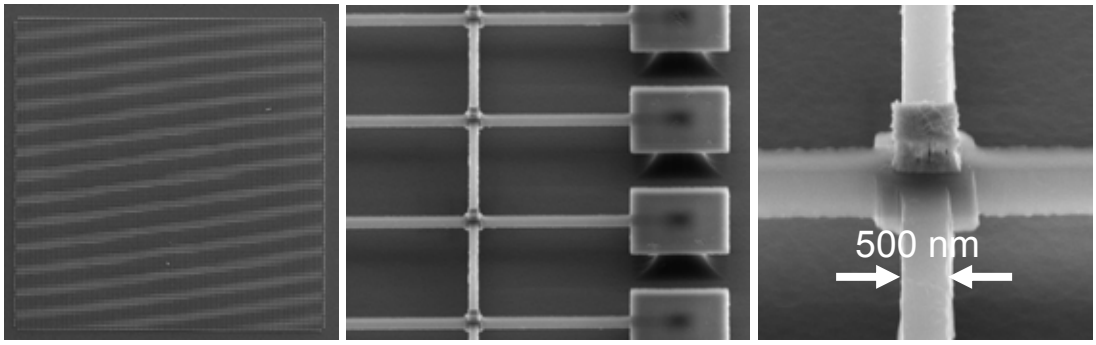

Fig. 7.3. A 100 × 100 coupled oscillator large array: (left) the complete 100 × 100 array (the dimensions are 1 mm × 1 mm), (middle) close-up of array edge, and (right) a single element showing the W island on top of the node.

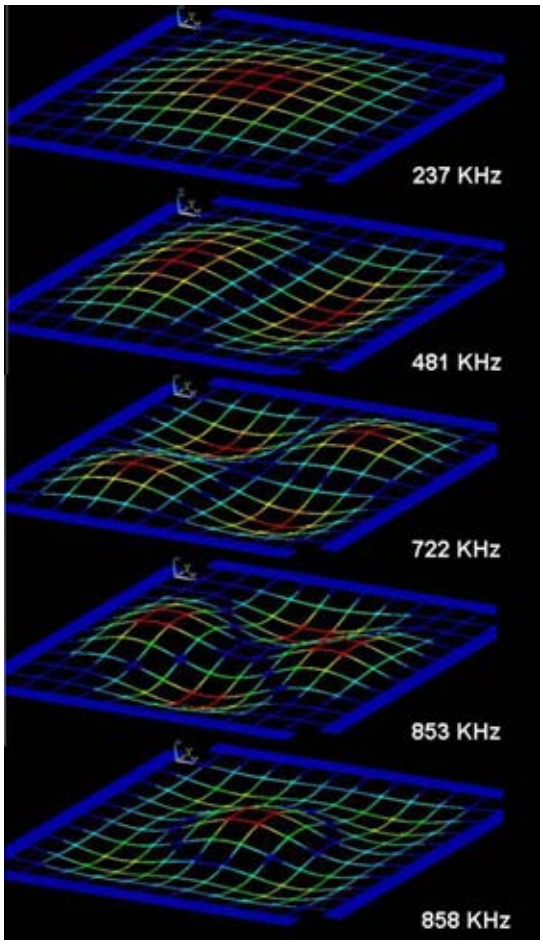

Fig. 7.4. Numerical analysis of the lowest frequency vibrational modes of the 10 × 10 coupled oscillator array.

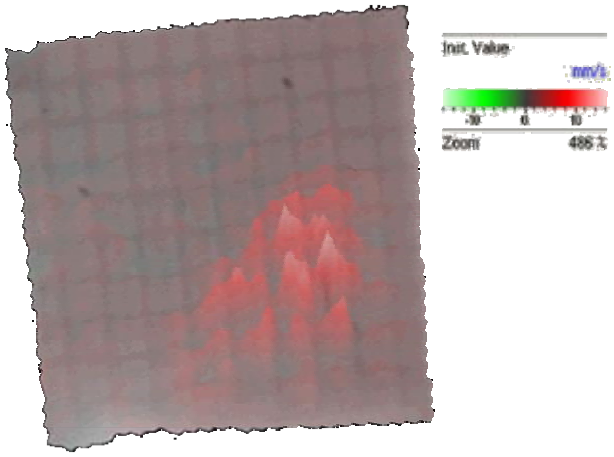

Fig. 7.5. The 2nd lowest vibrational mode of the 10 × 10 coupled oscillator array measured using laser Doppler vibrometry (courtesy of Polytec, Inc.). The mode has a diagonal nodal line and a resonance frequency of 486 KHz.

In addition to defect-free arrays, there is great interest in the characterization of coupled oscillator arrays containing intentional defects. Several types of defect structures can be intentionally introduced into the arrays. Controlled positional, mass, or spring constant disorder can easily be introduced by developing photolithographic masks with intentional randomness in the location of islands and spring elements and/or intentional randomness in the dimensions of the islands and springs. Alternatively, mass and spring disorder can be introduced subsequent to array fabrication through the use of focused ion beam (FIB) micromachining of specific array elements, e.g. etching away parts of some springs or islands. For introducing Q disorder in the array, a variety of methods are available [9]. One approach is to fabricate the oscillator array with polycrystalline Si springs, and then selectively amorphize some of the springs by focused ion beam irradiation, thus establishing low Q springs embedded in an array of high Q springs. Alternatively, electron-beam assisted chemical vapor deposition could be used to deposit chemical species on the surfaces of some of the springs, and thus increase the dissipation in those springs. One of the easiest ways to achieve this is through the use of focused electron beam exposure of select spring elements in an electron microscope of modest vacuum. This process leads to deposition of adventitious carbon species at the focus of the intense electron irradiation and would be expected to reduce the Q of the affected spring.

In order to understand the effects of disorder on mode localization in coupled oscillator arrays, simulations have been completed using ANSYS modeling. A 20 × 20 element array was chosen for the simulations with the array having the same mechanical characteristics (dimensions, materials, etc.) as our fabricated arrays. In order to simulate disorder, we took a 5 × 5 portion of the 20 × 20 array and applied a random displacement of the elements. (Previous studies on 1-D macroscopic systems have shown that positional disorder is a stronger driver for localization than mass disorder [5].) One way to visualize this localization is to look at the mode density of states in the disordered system vs. the ideal system. Fig. 7.6 shows the mode density of states for the ideal and defect-containing array. The plot clearly shows the effect of localization: there is a peak in the number of modes within a frequency range, whereas a peak is absent in the ideal case. Future work will be focused on obtaining experimental realization of this disorder-induced change in mode distribution (localization) using oscillator arrays that have

been fabricated to contain an intentional defect or defective area. These experiments will require spatial mapping of the resonance modes (e.g. laser Doppler vibrometry) to identify the onset of localized vibrational modes.

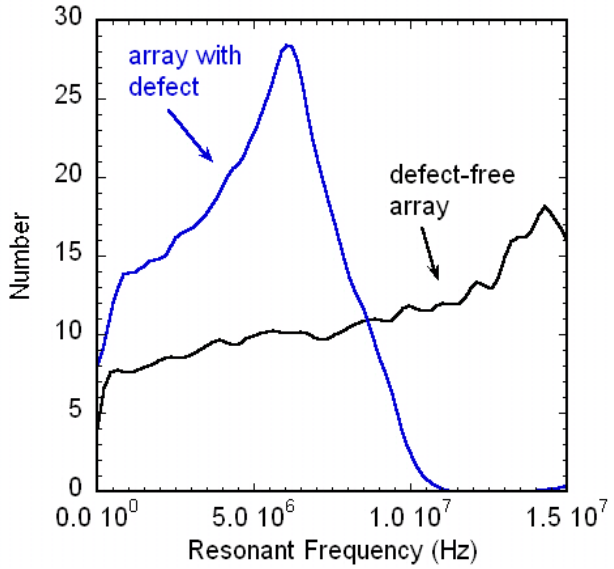

Fig. 7.6. Number of vibrational modes as a function of mode frequency for an ideal 20 × 20 array and a 20 × 20 array containing a disordered region. A peak is observed in the disordered array, consistent with localized vibrational modes.

7.4 Conclusions

Coupled oscillator arrays, including 1D arrays of cantilever oscillators and 2D arrays of nodes and springs, were fabricated out of amorphous and polycrystalline diamond materials. The 2D arrays were fabricated as square lattices of 10 × 10 and 100 × 100 elements having tungsten proof masses at each element. These arrays were fabricated to be ideal (free of defects), and experimental testing revealed a series of drumhead vibration modes. Simulations of arrays containing regions of disorder revealed that mode localization should be observable in defect-containing arrays. Studies to confirm localization in these mechanical systems have been undertaken.

Assistance in scanning electron microscopy by B. McKenzie, ANSYS modeling of vibrational states by M. Baker, and laser Doppler vibrometry by E. Lawrence (Polytec corporation) are gratefully acknowledged.

7.5 References

[1] P. W. Anderson, Phys. Rev. **109**, 1492 (1958).
[2] P. Dean and M.. D. Bacon, Proc. Phys. Soc. **81**, 642 (1963).
[3] S. John, Phys. Rev. Lett. **53**, 2169 (1984); T. R. Kirkpatrick, Phys. Rev. B **31**, 5746 (1985).
[4] M. L. Williams and H. J. Maris, Phys. Rev. B **31**, 4508 (1985).
[5] S. He and J. D. Maynard, Phys. Rev. Lett. **57**, 3171 (1986).

[6] While there can be significant variation in the size of the elements, the center of mass of those elements should lie close to expected lattice site.
[7] see, for example, Ping Sheng, *Scattering and Localization of Classical Waves in Random Media* (World Scientific Publishing, Singapore, 1990).
[8] M. Sato, B. E. Hubbard, A. J. Sievers, B. Ilic, D. A. Czaplewski, and H. G. Craighead, Phys. Rev. Lett. **90**, 044102 (2003).
[9] Formally, Q disorder is a special case of disorder in the complex modulus of elasticity, $E = E' + iE''$, viz. disorder in E'' while E' remains constant.

8.0 Future

In view of the importance of understanding internal dissipation in resonant micro- and nanomechanical systems, there is much further work that needs to be done to understand generic dissipation processes in small scale systems. Our work has shown that most internal dissipation in small systems is controlled by defect-related dissipation processes, and the number of active defects are far higher in amorphous systems compared to crystalline systems. Even for ideal crystalline systems, such as silicon, the dissipation processes are not well-understood. There are numerous studies in silicon that suggest that the dissipation is surface-dependent (presumably related to the presence of a surface oxide), but even when the oxide is removed, the dissipation does not drop to the intrinsic limit set by thermoelastic dissipation [1-4]. Therefore, even here, we expect defect-related dissipation processes to dominate.

On the basis of the work performed in this project, it is suggested that one of the most fruitful venues for future work is to perform atomistic simulations of defect-related internal dissipation in concert with experimental studies of the temperature-dependence of internal dissipation. Using this approach, we may expect to develop greater insight in the coupling of vibrational modes, defect relaxation processes, and phonon transport and scattering. All of these factors come into play in controlling the dissipation process, and some processes, such as phonon transport, are sample size scale dependent (there is a transition from diffusive to ballistic phonon transport as the phonon mean free path exceeds the sample dimension). Extending experimental measurements down to cryogenic temperatures would also greatly benefit these studies, as it would extend the range of relevant defect relaxation processes and greatly change the phonon populations in the material.

Another very important area for future work is the study of the dynamics of coupled oscillator systems. Our work on 1D and 2D coupled oscillator arrays has shown that these systems offer potential for advancing our understanding of emergent phenomena in collective systems, understanding non-linear dynamics in coupled systems, understanding mechanical dissipation processes, and developing sensor systems which exhibit greater response to a weak stimulus. Using simpler systems than those that we have fabricated, other researchers have discovered very interesting dynamics in systems of resonant mechanical systems and have begun to apply these ideas for sensing concepts [5-7]. With the addition of a newly acquired scanning laser Doppler vibrometry system at Sandia, we expect to develop unique systems of coupled mechanical oscillators for basic research studies and the development of advanced sensors.

8.1 References

[1] D. W. Carr, S. Evoy, L. Sekaric, H. G. Craighead, and J. M. Parpia, Appl. Phys. Lett. **75**, 920 (1999).

[2] J. Yang, T. Ono, M. Esashi, Sens. Actuators **82**, 102 (2000).

[3] K. Y. Yasumura, T. D. Stowe, E. M. Chow, T. Pfafman, T. W. Kenny, B. C. Stipe, and D. Rugar, J. Microelectromech. Systems **9**, 117 (2000).

[4] J. Yang, T. Ono, M. Esashi, J. MEMS **11**, 775 (2002).

[5] R. L. Badzey and P. Mohanty, Nature **437**, 995 (2005).

[6] A. Gaidarzhy, G. Zolfagharkhani, R. L. Badzey, and P. Mohanty, Phys. Rev. Lett. **94**, 030402 (2005).

[7] M. Sato, B. E. Hubbard, and A. J. Sievers, Rev. Modern Phys. **78**, 137 (2006).

9.0 Acknowledgments

In addition to those individuals acknowledged separately in prior sections of this report, we would also like to acknowledge valuable discussions and input from D. W. Carr, B. E. N. Keeler, and W. Pan. This work was supported by a Laboratory Directed Research and Development project at Sandia National Labs, Albuquerque, NM. Sandia is a multiprogram laboratory operated by Sandia Corp., a Lockheed Martin Co., for the U.S. Dept of Energy's National Nuclear Security Administration under contract DE-AC04-94AL85000.

DISTRIBUTION

1	MS 0123	D. L. Chavez, LDRD Office, 1011
1	MS 1069	D. A. Czaplewski, 1749-2
1	MS 1082	J. R. Wendt, 1725
5	MS 1304	J. P. Sullivan, 1132
1	MS 1415	N. A. Modine, 1132
1	MS 1415	D. E. Peebles, 1112
1	MS 1415	R. Hwang, 1110
1	MS 1415	T. A. Friedmann, 1112
1	MS 1427	J. M. Phillips, 1100
2	MS 0899	Technical Library, 4536
2	MS 9018	Central Technical Files, 8944